# 5

# Macroscopic Interactions— Particle Absorption and Scattering

The tiny vibrations of the electrons of atoms and molecules, when exposed to electromagnetic radiation, are fundamental to the way radiation interacts with matter. The ability of condensed matter to produce these vibrations is characterized by the optical properties discussed in the previous chapter. Optical properties alone, however, do not provide us with a complete description of these interactions. Further complications arise by the way these tiny vibrators are arranged to make up particles. For instance, changing the macroscopic structure of a solid sheet of glass by smashing it into a fine powder, results in a dramatic change in the visual appearance of the material and, therefore, in the way radiation interacts with the glass, despite the fact that the composition of both configurations is identical. We can view a small piece of this powdered glass as being composed of a large collection of tiny oscillating dipoles as schematically portrayed in Fig. 5.1. These dipoles, oscillating at the frequency of the applied electromagnetic field, produce a secondary field that radiates out in all directions (we will call this the *scattered* field). Particle scattering is a complex problem because the secondary waves generated by each dipole also act to stimulate oscillations in neighboring dipoles. Thus radiation scattered out from the particle in a particular direction, say to point P, is a superposition of all the scattered wavelets and the precise details of this superposition depend on the way dipoles are arranged to form a particle.

Particle scattering is germane to many atmospheric remote sensing problems, from radar estimates of rainfall, to the estimation of cloud droplet size from the measurement of solar radiation reflected by clouds. This chapter discusses the scattering and absorption properties of particles and attempts to build up an understanding of these properties by first considering scattering by a single radiating dipole. The scattering properties of larger particles, formed as an arrangement of many individual dipoles, is considered later in the chapter.



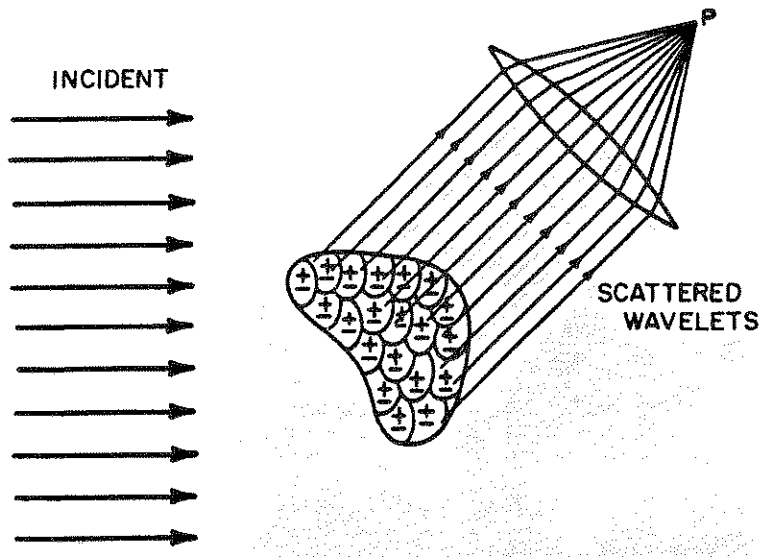


**Figure 5.1** The radiation scattered by a particle and observed at P results from the superposition of all wavelets scattered by the subparticle regions (dipoles) (from Bohren and Huffman, 1983.)

## 5.1 A Single Oscillating Dipole: Rayleigh Scatter

A logical place to begin a discussion of particle scattering is to consider the radiation scattered by a single oscillating dipole. We might consider an individual dipole as a small spherical particle, much smaller in comparison to the wavelength of the incident radiation, and refer to the scattering by such a particle as *Rayleigh scattering*, after Lord Rayleigh, who first described the properties of scattered sunlight by air molecules. In fact, an understanding of Rayleigh scattering has more than just heuristic appeal as it applies to many scattering phenomena of relevance to the atmosphere. Rayleigh scattering describes how visible radiation is scattered by atmospheric gases, how the longer wavelength infrared radiation is scattered by aerosol particles a few tenths of a micron in size, and how the even longer microwave radiation is scattered by cloud droplets and small rain drops. The properties of Rayleigh scattering have been exploited in both active and passive remote sensing applications. Rayleigh scattering is used directly in the analysis of weather radar (Chapter 8) and exploited in microwave sensing of cloud water (Chapter 7).

The backscatter of ultraviolet radiation by $O_2$ and $N_2$ is described by Rayleigh scattering and is important in the estimation of atmospheric ozone using observations from satellites (Chapter 6) as well as in the calibration of the backscatter of laser radiation in lidar systems (Chapter 8).

We start with a spherical particle small enough that the electric field within the particle is constant. This single spherical dipole oscillates under the influence of an oscillating electric field. This field has two orthogonal components: one parallel and the other perpendicular to a particular *plane of reference*. According to (4.1), each component of the electric field, in turn, induces a dipole moment parallel to the incident electric field. Figure 5.2 provides a reference to the geometry of the interaction under discussion. The components of the electric fields and the associated dipole moments are, respectively, represented by $\mathcal{E}_{\ell,r}$ and $P_{\ell,r}$ and are defined relative to the plane of reference. This plane contains the directions of propagation of both the incident and the scattered radiation.[1] The angle formed by these directions, represented as $\Theta$ in Figs 5.2 and 5.3, is referred to as the *scattering angle*.

We may visualize the dipole, defined by its moment $P_r$, as a line of fixed length separating two charges (as in Fig. 2.2). In this case, the line is perpendicular to the plane of reference and its length remains unchanged when viewed by an observer who moves around the particle on the plane of reference. Thus, the vertical (or perpendicular) component of the dipole moment and the vertically polarized component of the electric field is independent of $\Theta$. Using the same arguments, the magnitude of the dipole that lies parallel to the plane of reference varies with the direction of observation and disappears completely when viewed end on at $\Theta$ =90 degrees. Based on these simple geometric considerations, the horizontal (or parallel) component of the electric field varies as $\cos\Theta$. The two components of the electric field are therefore

$$\mathcal{E}_r = \mathcal{E}_{or}[\frac{e^{-ik(R-ct)}}{R}]k^2\alpha$$
$$\mathcal{E}_\ell = \mathcal{E}_{o\ell}[\frac{e^{-ik(R-ct)}}{R}]k^2\alpha\cos\Theta \qquad (5.1)$$

where $\mathcal{E}_{or}$ and $\mathcal{E}_{o\ell}$ are the respective amplitudes of the fields incident on the particle, $\alpha$ is the polarizability introduced in Section 4.1, $k$ is the wavenumber, and where radiation scattered by a single oscillating dipole is a spherical wave expressed by the factors in parentheses. The two intensity components of polarized radiation therefore take the form

$$I_r = I_{or}k^4 \mid \alpha \mid^2 /R^2$$
$$I_\ell = I_{o\ell}k^4 \mid \alpha \mid^2 \cos^2\Theta/R^2 \qquad (5.2)$$

A special and important case applies to an unpolarized beam of radiation, like sunlight, scattered by small particles. Unpolarized radiation can be viewed as a mixture of two independent linearly polarized beams of the same intensity. Therefore, $I_{or} = I_{o\ell} = I_o$, and

$$I = \frac{1}{2}(I_\ell + I_r) = I_o[1+\cos^2\Theta]k^4 \mid \alpha \mid^2 /R^2 \qquad (5.3)$$

[1] The scattering plane remains arbitrary for both forward scattering ($\Theta = 0$ degrees) and backscattering ($\Theta = 180$ degrees) and thus requires an additional direction to define this plane. Radar studies, for example, define the scattering plane as the plane that contains both the transmitted and received beams and the local vertical. The polarization parallel to this plane is then referred to as vertical polarization even though this component might not actually point along the vertical direction. In some lidar applications, the scattering plane is defined as the plane containing both the transmitted and received beams and the direction of the (linear) polarization of the transmitted beam (refer to section 5.7 for further discussion).



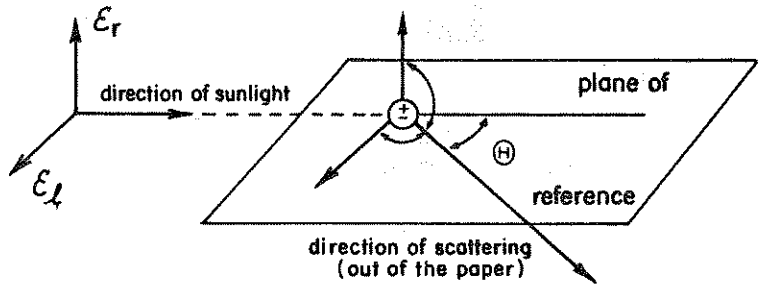


**Figure 5.2** Geometry for scattering by a single dipole. The plane of reference and the orthogonol components of both the electric field and the dipole moment which lie parallel and perpendicular to the plane are shown. The scattering angle $\Theta$ is defined on this plane.

describes the scattered intensity of unpolarized radiation by small particles. The scattering pattern predicted by (5.3) is shown in Fig. 5.3a. The polarized components of the intensity, expressed by (5.2), are shown as dashed curves. The two independent beams that compose the incident radiation are scattered in unequal portions by a small sphere with the greatest difference occurring at scattering angles of 90 degrees where the parallel component of the scattered beam completely vanishes. In this way, the originally unpolarized incident light becomes polarized by scattering. At $\Theta$ =90 degrees, the scattered light is completely polarized along the direction perpendicular to the scattering plane whereas the light is unpolarized at $\Theta$ =0 degrees and has a mixture of parallel and perpendicular polarizations at other scattering angles. This amount of polarization is conveniently expressed in the form of the following ratio

$$LP(\Theta) = \frac{I_r - I_\ell}{I_r + I_\ell} \tag{5.4}$$

which is referred to as the *degree of linear polarization* (refer to Table 2.1). Substitution of (5.2) into (5.4) provides

$$LP(\Theta) = \frac{\sin^2 \Theta}{1 + \cos^2 \Theta} \tag{5.5}$$

which is shown in the form of a polar diagram in Fig. 5.3b. Since the scattered light is completely polarized at $\Theta$ =90 degrees, then $LP = 1$ in that direction. The points on the scattering plane for which $LP = 0$, in this case at $\Theta$ =0 degrees and $\Theta$ =180 degrees, are special and are referred to as *neutral points.*

Scattering of visible light by a pure molecular atmosphere is described by Rayleigh scattering. This scattering, according to Figs. 5.3a and b, polarizes sunlight. Based on the pattern displayed in Fig. 5.3b, the degree of polarization is expected to be greatest at 90 degrees to the sun and least when viewed directly toward and away from the sun. Actually the positions of the neutral points vary from these theoretical positions and the maximum degree of polarization never reaches 100 %. One of the reasons for these departures from theory is due to the effects of multiple scattering. Multiple scattered light is a mixture of waves that have been scattered a different number of times. Each time a scattering occurs, the radiation acquires a different degree of polarization depending on the direction of the scattering. Mixing multiply scattered waves leads to a



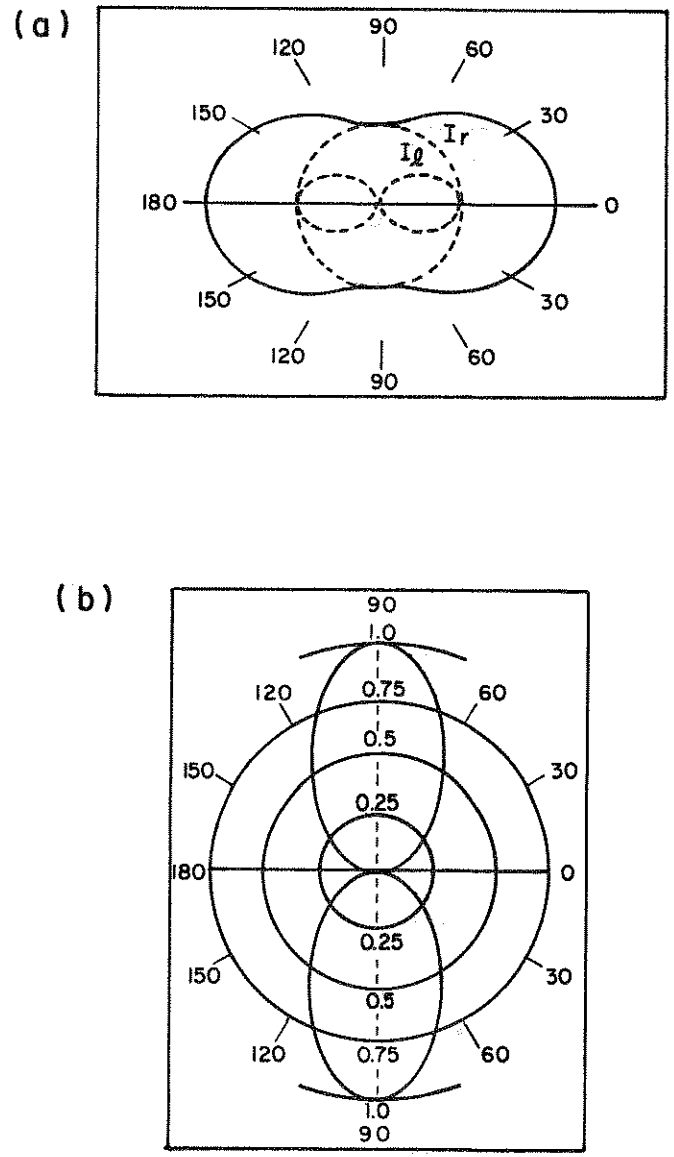


**Figure. 5.3** (a) The scattering pattern of a Rayleigh particle for unpolarized incident radiation. The parallel and perpendicular components are shown as dashed curves. (b) The angular distribution of the degree of polarization of radiation scattered by a Rayleigh particle for the case of unpolarized incident radiation.

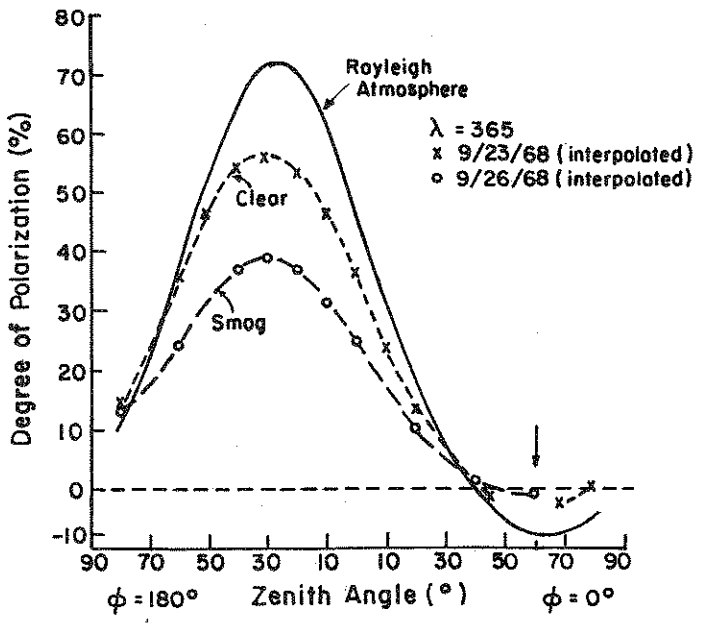


**Figure 5.4** The degree of polarization of skylight as a function of zenith angle for a sun elevation of 30 degrees from measurements at $\lambda$=0.365 $\mu$m for clear and smoggy conditions. The more aerosol, the greater is the multiple scattering, and the less distinct is the maximum of the degree of polarization (from Coulson, 1988).

decrease in the degree of polarization. Figure 5.4 provides an example of how much multiple scattering reduces the maximum degree of polarization in a pure Rayleigh atmosphere. Other factors, such as the scattering by non–Rayleigh particles, also reduce the degree of polarization because of the intrinsic scattering properties of these particles and the multiple scattering between these particles.

Multiple scattering also alters the pattern of polarized skylight, producing three neutral points (Fig. 5.5) instead of the predicted two points. These three points are the *Babinet* point, the *Brewster*, point and the *Arago* point. The positions of these in the sky can be predicted using a suitable model of multiple scattering and are a function of the amount of scattering material in the atmosphere. Since multiple scattering is produced both by air molecules and by the aerosol particles in the Earth's atmosphere (thick clouds provide an extreme example of multiple scattering), then the change in



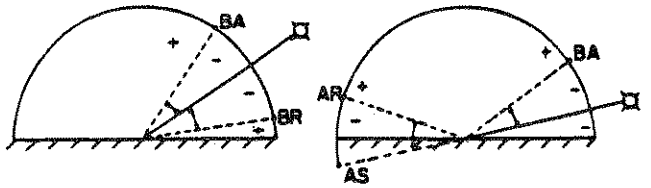


**Figure 5.5** A schematic diagram showing the positions of the neutral points of Babinet (BA), Brewster (BR), and Arago (AR). The plane of the paper represents the principal plane of the sun and the antisolar point is denoted as AS.

the position of the neutral points from their normal positions deter mined for a pure molecular atmosphere is indicative of the amoun of aerosol in the atmosphere (i.e., the *turbidity*, which is a concep discussed in more detail in Section 6.1). Measurement of the shif of the Arago point, for instance, has been proposed as a way o quantitively deducing atmospheric turbidity (Coulson 1983).

## *Excursus: Haidinger's Brush*

It is difficult to believe that we can see with our naked eye, un aided by any instrument, both polarized skylight and the directio of this polarization. It does, however, require some practice and certain amount of cunning. We begin by observing the twilight sk at 90 degrees from the setting sun. As we observe this region o sky almost directly above us for a minute or two, a kind of marbl effect appears. This is followed by a remarkable feature known a "Haidinger's brush," which resembles the illustration in Fig. 5.6 It is a yellowish brush with a small blue cloud on either side. Th yellow brush is perpendicular to the direction of light vibration an appears as a consequence of the polarization of skylight. Haidinger' brush takes some practice to see (Minneart, 1954) as the brushe fade rapidly due to the adjustments made by our eye. The reaso the brushes appear is a result of the dichroism of the yellow spot o our retina.

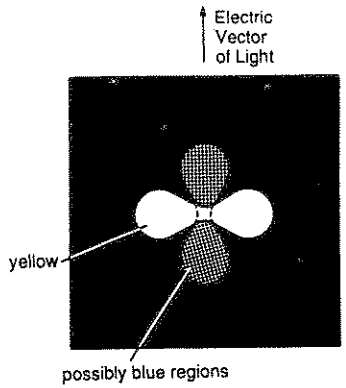


**Figure 5.6** Haidinger's brush is a remarkable feature that can be seen in the blue sky and is an indication of the polarization of skylight. The light brush is yellowish and the clouds at each side are blue (Minneart, 1954). The brushes tend to get lost in a cluttered background, so viewing an illuminated white sheet of paper through a linear polarizer (like that used for sunglasses) works well. The size of the pattern is about 3/4 in. across when viewed at normal reading distance (about 18 in.).

## 5.2 Radiation from Multiple Dipoles

Whereas an understanding of the interaction of electromagnetic waves by small particles is relevant to many remote sensing applications, scattering by particles comparable in size to, or larger than, the wavelength of the incident plane wave is perhaps relevant to an even more diverse range of topics. In this section we will consider the radiation field scattered by two neighboring dipoles as an analogy to scattering by such particles. This provides us with a simple, but conceptually rich, view of particle scattering and offers a framework for extending the discussion to even larger particles composed of more than two dipoles.

### 5.2.1 Scattering by Two Isolated Dipoles

Consider the simple hypothetical case of two identical dipoles separated by some distance $r$ as in Fig. 5.7. Suppose that these dipoles radiate independently of one another and consider radiation scattered along some direction defined by the scattering angle $\Theta$. The phase difference $\Delta\phi$ between the two scattered waves at some point P is simply the result of the difference in the path length



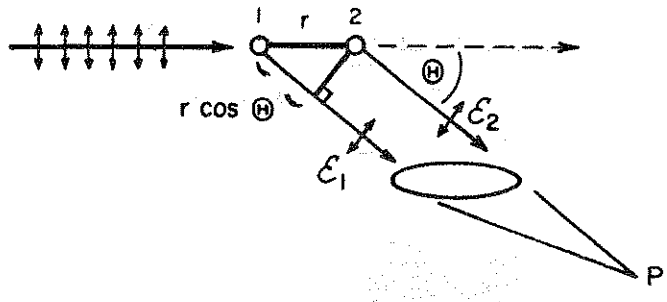


**Figure 5.7** Two isolated dipoles emit waves in all directions. At some point P far from the "particle," these waves superimpose to create the scattered wave along the direction $\Theta$. These waves either constructively or destructively interfere depending on their relative phase difference $\Delta\phi$.

traversed by one wave relative to another, that is

$$\Delta\phi = x\,(1 - \cos\Theta) \tag{5.6}$$

where $x = 2\pi r/\lambda$ is a quantity that is hereafter referred to as the *size parameter*. The two waves superimpose at some distance from the 'particle' to produce a field

$$\mathcal{E}_{1+2} = \mathcal{E}_1 e^{i\phi} + \mathcal{E}_2 e^{i\phi+\Delta\phi} \tag{5.7}$$

Suppose the detector that receives this scattered radiation has a time constant which is long enough that at least one full cycle of the oscillation is sampled. Then integration of (5.7) over a complete cycle produces a detected intensity of the form

$$I_{1+2} = B[\mathcal{E}_1^2 + \mathcal{E}_2^2 + 2\mathcal{E}_1\mathcal{E}_2\cos\Delta\phi], \tag{5.8}$$

where $B$ is a constant. If $\mathcal{E}_1 = \mathcal{E}_2$, then the two fields exactly cancel when $\Delta\phi = \pi, 3\pi, ...$; that is they are exactly out of phase. On the other hand, for $\Delta\phi = 0, 2\pi, 4\pi, ...$, the two fields reinforce each other exactly and are in phase. In both cases, the "scattering" is said to be *coherent*. But the phase difference depends on both the separation of the dipoles and the direction of scatter. For an arbitrarily shaped particle, the value of $\Delta\phi$ may vary in an arbitrary way except

when $\Theta = 0°$ (i.e. except in the forward direction). The scattered radiation at $\Theta \neq 0°$ is thus a result of complex superpositions of waves of many different relative phase differences (Fig. 5.8a). The forward direction, however, is special as the fields at the detector remain in phase. For two dipoles the intensity in this direction is four times that of the incident wave (Fig.5.8b). Hence a particle of $N$ such oscillators produces light in this forward direction that has an intensity proportional to $N^2$. It follows that scattering by large particles is predominantly in the forward direction and more so as the particle size increases. The situation is much more complicated in the backwards direction. Scattering does not increase nearly so rapidly with an increase in the number of dipoles since not all dipoles are in phase. Furthermore, the phase difference depends on the scattering direction and the scattering pattern (that is the scattered intensity as a function of $\Theta$) undergoes excursions from a maximum in the forward direction through one or more minima as $\Theta$ varies and the number of these minima depends on the separation of the two dipoles.

The arguments presented here for two dipoles extend to a huge array of them and thus to a larger particle. The larger the particle, the more it scatters forward and the greater the forward to backward asymmetry. Also, the larger the particle, the more complicated is the pattern of scattered light. Returning to our simple two dipole particle, we note that when the phase difference between two scattered waves is an odd multiple of $\pi$, the two waves are out of phase producing a zero intensity at the scattering angle that produces these phase differences. We infer from this that as $x$ increases the number of null points in the scattering pattern increases.

So far, the effects of interactions among the dipoles have been ignored. These interactions complicate matters but do not change the nature of our discussions substantially. The expectations about particle scattering arrived at here are supported by detailed calculations from a more precise theory (such as from the Lorenz–Mie theory described later). Example calculations from this theory are shown in Fig. 5.9 in the form of polar plots of the perpendicular and parallel components of the intensity of the light for scattering by different sized water droplets (represented by different values of $x$). For small size parameters ($x < 1$; not shown), the Rayleigh scattering patterns predicted by (5.2) are obtained. Deviations from Rayleigh scatter appear as $x$ increases producing forward to backward asymmetries in both $I_r$ and $I_\ell$. The scattering pattern of a



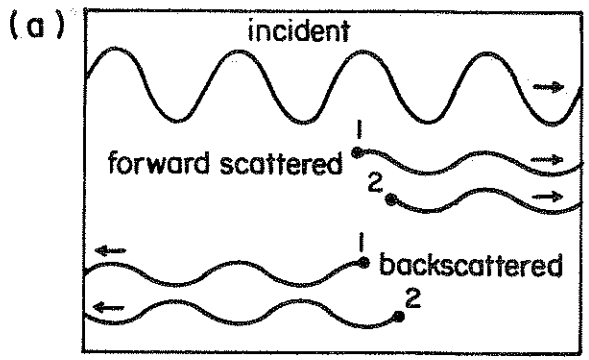


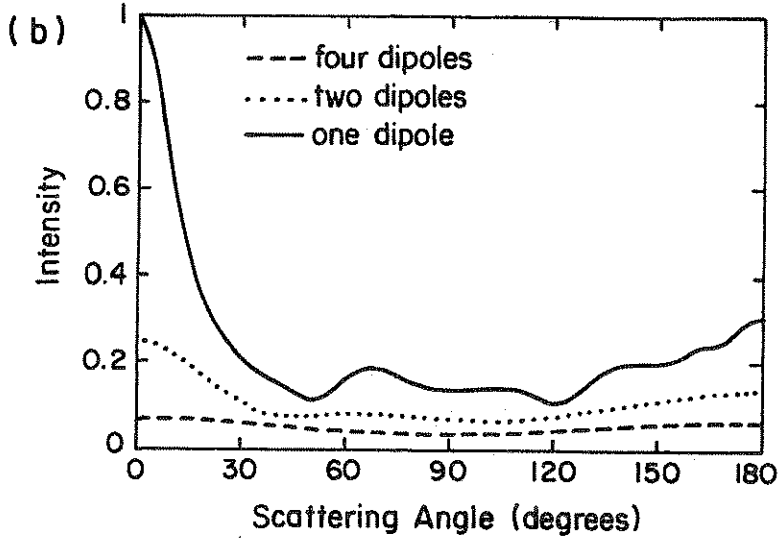


**Figure 5.8** (a) Excited by an incident wave, two dipoles scatter in all directions. In the forward direction, the two waves are exactly in phase regardless of the separation of dipoles. (b) The greater the number of dipoles in the particle array, the more they collectively scatter toward the forward direction. For the example shown here all dipoles lie on the same line and are separated by one wavelength and interact with each other. The scattered intensity is obtained as an average over all orientations of the line of dipoles (from Bohren, 1987).

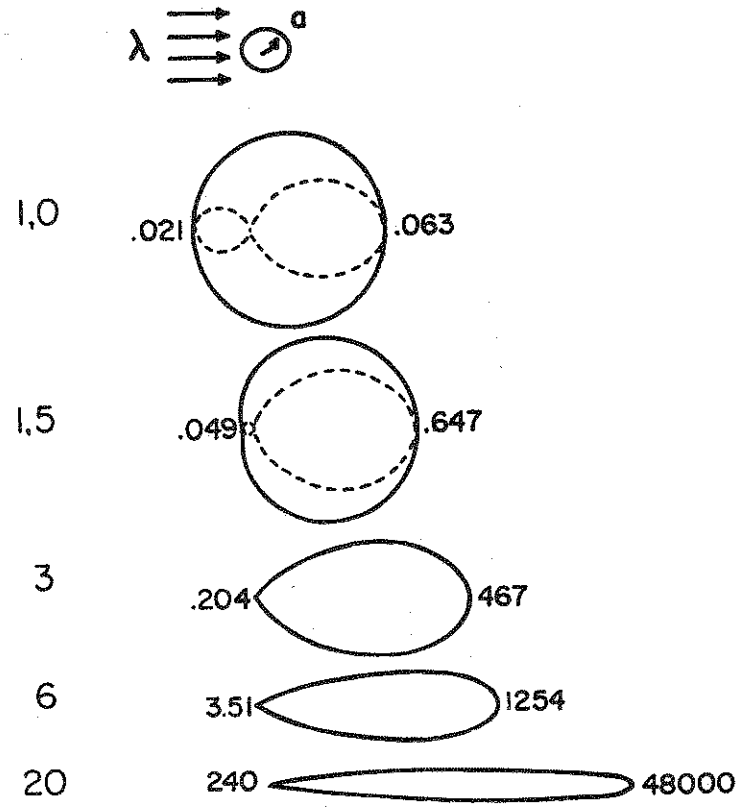


**Figure 5.9** Polar plots of the scattered intensity for selected values of the size parameter. The numbers indicate relative magnitudes in the forward and backward directions. Note the scale change (Bohren and Huffman, 1983).

large particle represented in this diagram at $x = 20$ is dominated by a large forward scattering lobe and has a much more complicated shape. For 10$\mu$m cloud droplets, the size parameter $x$ corresponding to visible light of wavelength 0.6$\mu$m is about 100 so scattering of this radiation is mainly in the forward direction.

## *Excursus: Phased–Array Antennas*

A very practical application of dipole array scattering is provided in the example of a dipole antenna array. We mentioned in Chapter 2 how a single dipole, radiating at microwave frequencies, can be constructed. Let us suppose now that we have a linear array of $N$



independent dipoles as shown in Fig. 5.10a. The contribution of the $n$th radiator to the total far field along the direction $\Theta$ is

$$\mathcal{E}_n \sim (a_n e^{i\phi_n}) e^{-ikd_n \sin\Theta} \tag{5.9}$$

and the total field, which is the sum of each dipole field, is

$$\mathcal{E}(\Theta) \sim \sum_{n=1}^{N} a_n e^{i\phi_n - ikd_n \sin\Theta} \tag{5.10}$$

where $a_n$ is the relative amplitude of the signal radiated by the $n$th element and $\phi_n$ is its phase. If all the radiators are identical in both amplitude and phase, and equally spaced, then the total far field emitted by the array is

$$\mathcal{E}(\Theta) \sim a e^{i\phi} \sum_{n=1}^{N} e^{-inkd\sin\Theta} \tag{5.11}$$

which we represent as a vectorial sum of $N$ equal vectors each separated by a phase $\Delta\phi = kd\sin\Theta$. As seen in Fig. 5.10b, the sum is strongly dependent on the value of $\Delta\phi$. For example, with $\Theta = 0°$ and $\Delta\phi = 0$, all vectors add coherently just as in our example of forward scattering by particles. As $\Delta\phi$ increases, the vectors are out of phase relative to each other, leading to a decrease in the total sum. Where $\Delta\phi$ is such that $N\Delta\phi = 2\pi$, the sum is then equal to 0. This corresponds to

$$Nkd\sin\Theta = 2\pi \tag{5.12}$$

or

$$\Theta = \sin^{-1}\frac{2\pi}{Nkd} \tag{5.13}$$

At this angle, there is a null in the total radiated field and the shape of the field between the null points is referred to as the *lobe*. These occur when $N\Delta\phi = 2m\pi$ for integer values of $m$, leading to a series of nulls at

$$\Theta = \sin^{-1}\frac{2m\pi}{Nkd} \tag{5.14}$$

Peaks that lie between these nulls correspond to the condition

$$N\Delta\phi = 2m\pi + \pi \tag{5.15}$$

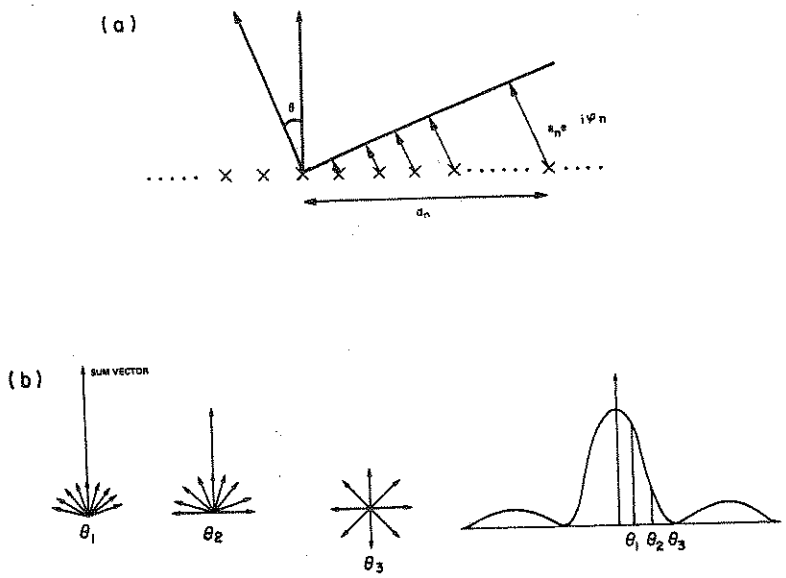


**Fig. 5.10** (a) The geometry of a linear array of oscillators. (b) The radiation pattern emitted from a linear array of oscillators shown in vector form and as a function of angle $\Theta$. One of the main challenges of antenna design is to minimize the side lobes and keep the main lobe as narrow as possible.

and to the angle

$$\Theta = \sin^{-1} \frac{(2m+1)\,\pi}{Nkd} \tag{5.16}$$

Suppose the linear array of dipoles is used to direct a beam to a target $P$ that is not vertically above the antenna. Depending on the mechanism of combining the signal from each antenna, the array can be focused or unfocused on our target of interest. By engineering a specific phase difference between each dipole, which is done electronically in modern systems, we are able to steer the beam along a chosen direction.

We also pointed out previously that the radiation emitted from a dipole antenna will be linearly polarized. The orthogonal components of polarization are obtained when two linear arrays of radiating dipoles are placed perpendicular to one another. This configuration is typical of the wind profiling antenna systems used to measure atmospheric wind and is described further in Chapter 8.



### 5.2.2 The Discrete Dipole Approximation

Scattering of electromagnetic radiation by irregularly shaped particles is a topic of relevance to many atmospheric remote sensing problems. Unfortunately, our ability to solve Maxwell's equations precisely and thus compute the scattering and absorption properties of atmospheric particles is limited to very idealized geometries (i.e., spheres, circular cylinders, and spheroids). A number of approximate methods for calculating scattering by nonspherical particles exist. One approach, developed to study the scattering of starlight by interstellar dust grains, is the discrete dipole approximation (DDA). The basic concept, which was first introduced by Purcell and Pennypacker (1973), may be viewed as a generalization of the ideas presented earlier in our discussion of a two–dipole particle.

We can attempt to understand the concept of the DDA by considering the situation shown in Fig. 5.11 where an incident field $\mathcal{E}_{in}$ is scattered by a particle composed of many dipoles. A response field $\mathcal{E}_{res}$ is then created by this scattering which we imagine to be very far from the particle at $P$. $\mathcal{E}_{res}$ at $P$ is the (vector) sum of the fields produced by the external source and the fields produced by each of the dipoles in the particle, that is

$$\mathcal{E}_{res} = \mathcal{E}_{in} + \sum_{dipoles} \mathcal{E}_{dipoles} \tag{5.17}$$

The electric field at each dipole, defined by the position index $j$, is characterized in terms of the dipole moment

$$p_j = \alpha_j \mathcal{E}_{dipole,j} \tag{5.18}$$

according to (4.2). The field at each dipole results from the superposition of the external field from our source at $S$ with the fields associated with the other $N-1$ dipoles. That is

$$p_j = \alpha_j [\mathcal{E}_{in,j} - \sum_{j \neq k} A_{jk} p_k,] \tag{5.19}$$

where $-A_{jk}p_k$ is the contribution to the electric field at dipole position $j$ due to the dipole oscillating at position $k$. The precise form of $A_{jk}$ does not need to concern us and the interested reader should

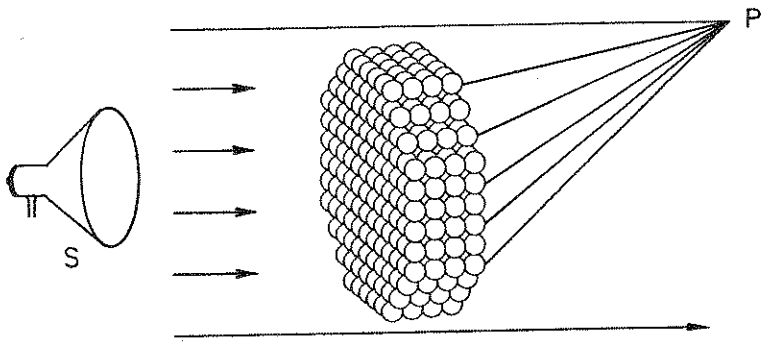


**Fig. 5.11** A hexagonal plate particle represented by 480 dipoles. Incident light from a source $S$ is scattered by the particle to produce a response field at $P$. This response field has a component that is represented by the superposition of the fields from each dipole. The complication arises from the mutual interference of the dipoles producing a distortion of the incident field.

attempt Problem 5.6 as well as consult the references given at the end of this chapter to learn more about the DDA.[2]

The DDA method solves (5.19) for all $p_j; j = 1, \ldots, N$ by rearranging this equation in matrix form which is explored further in Problem 5.6. The details are omitted here, but it is relevant to note that this involves solution of a $3N \times 3N$ complex matrix. As a rough guideline, the size $d$ of the individual dipoles needed to represent the particle follows from

$$|\,\mathrm{m}\,|\, kd < 1/3$$

[2] Equation (5.19) is actually a numerical simplification of the integral solution to Maxwell's equations. The summation term represents a discretization of the integral

$$\nabla \times \nabla \times \int_V [\epsilon(\vec{r'}) - 1]\mathcal{E}(\vec{r'})G_o(\vec{r}, \vec{r'})dV'$$

where $G_o(\vec{r}, \vec{r'})$ is the free space Green's function, the integral is carried out over the entire volume of the particle, and the curl operator, $\nabla\times$, is from standard vector calculus (e.g., Arfken 1985).



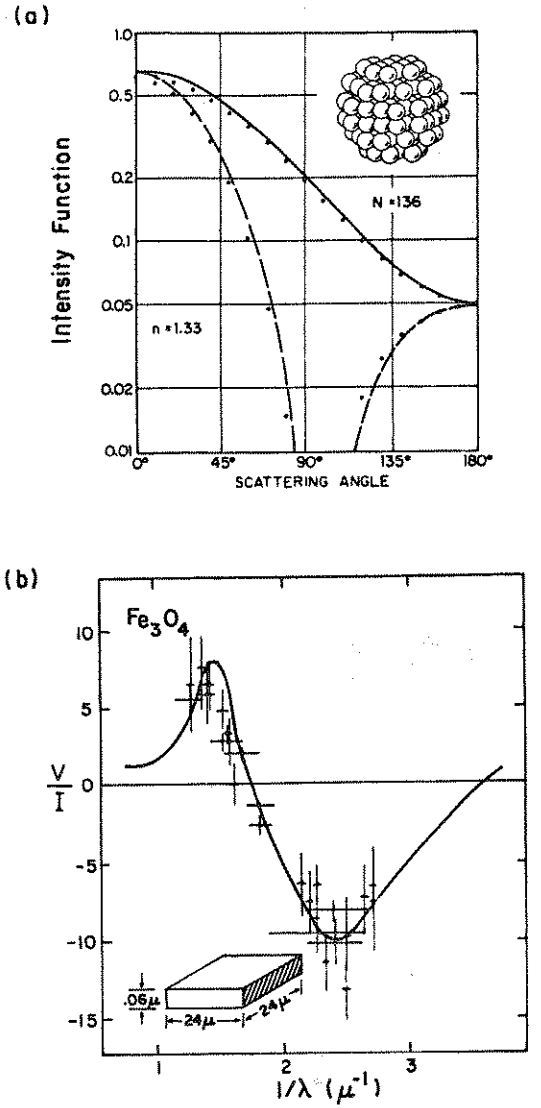


**Figure 5.12** (a) Scattered light (arbitrary units) as a function of scattering angle for a dielectric sphere with $x = 1.5$, m$=1.33$. The curves correspond to Lorenz–Mie solutions, the points to DDA solutions for a "sphere" consisting of 136 dipoles. Solid curve – scattering normal to electric field; dashed curve – scattering normal to the magnetic field (after Purcel and Pennypacker 1973). (b) DDA derived circular polarization V/I for magnetite platelets of the size given. Plotted are circular polarization observations (after Shapiro, 1975).

or

$$d < \frac{\lambda}{6\pi \mid \mathrm{m} \mid}$$

where $\lambda$ is also expressed in micrometers. For example, scattering of 0.5 $\mu$m radiation by a water sphere of radius 1 $\mu$m can be calculated to better than 5% accuracy when represented by a "sphere" of 65,400 dipoles.

The matrix that must be inverted to solve (5.19) rapidly becomes large as the size parameter increases. An example of a scattering calculation for a sphere composed of 136 dipoles is shown in Fig. 5.12a. The curves in this diagram provide a measure of the scattered intensity as a function of scattering angle which is defined in two planes: one normal to the electric field (solid curve); the second normal to the magnetic field (dashed curve). Other parameters are defined on the diagram. The curves represent the scattering from spheres as derived from the Lorenz–Mie scattering solution (Section 5.6) and the points are the results of calculations obtained using the DDA approach for the sphere represented by the cluster of dipoles shown in the inset. Figure 5.12b is a diagram of the degree of circular polarization (refer to the discussion of Table 2.1 for the definition of this parameter) derived from the DDA calculations for a magnetite platelet shown in the inset and plotted as a function of wavelength. These calculations are compared to actual observations of the circular polarization of starlight. One of the most important properties of interstellar scattering of starlight is the way this light is polarized. For dust grains to polarize light, they must be nonspherical in shape and collectively aligned in some organized fashion. The predicted behavior of $V/I$ by DDA is at least consistent with the idea that these dust grains are flat, oriented platelets of magnetite.

## 5.3 Particle Extinction

The special properties of forward scattering have already been noted. Scattering in this direction is also a measure of the totality of the interaction between the radiation and the particle. To illustrate how forward scattering is used in such a way, suppose that particles exist between a source of radiation like the sun and a detector like that flown on a satellite (Fig. 5.13). The detector receives less radiation when particles or molecules exist along the path to attenuate the radiation than when no particles or molecules are present. The incident beam is said to have undergone *extinction* or *attenuation* when



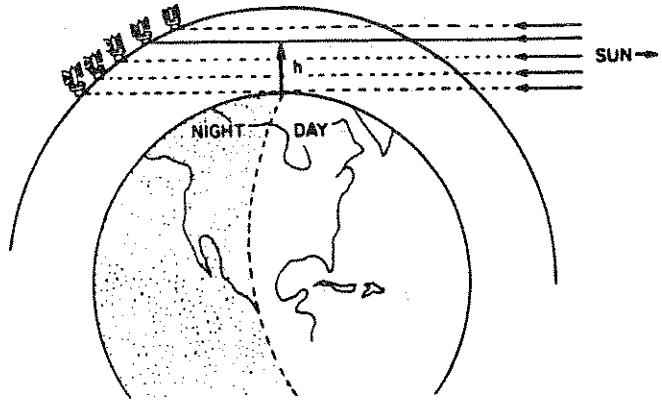


**Figure 5.13** A sunset as viewed by the SAGE instrument on the Nimbus 7 satellite. The instrument starts to scan the solar disk at a tangent height $h$ and follows it down until the sun disappears. Different layers are successively sampled during the event (McCormick et al., 1979).

such a reduction occurs. A number of both active and passive remote sensing methods make use of direct extinction by both particles and molecules as discussed further in Chapter 6.

### *Excursus: Extinction–It is Black and White*

The experimenter who observes radiation scattered in the forward direction, as for the example considered earlier, cannot determine if the radiation is decreased because it is absorbed or decreased because it is scattered. A simple illustration of this elementary point is well described by Bohren (1987) and is highlighted in Fig. 5.14. One cannot distinguish between the images of two water–filled glass petri dishes projected on a screen, yet their darkness arises from different mechanisms. Light incident on the inky water is attenuated mainly by absorption, whereas light incident on the milky water is mostly scattered. It is only by looking at the dishes that this difference between them becomes apparent. An important scattering parameter that helps quantify these differences is the ***single scattering albedo*** $\tilde{\omega}_o$. This parameter is the ratio of the amount of scattering that attenuates the light to the total extinction (absorption ***plus*** scattering). For the milky water, $\tilde{\omega}_o \approx 1$ since light is primarily scattered

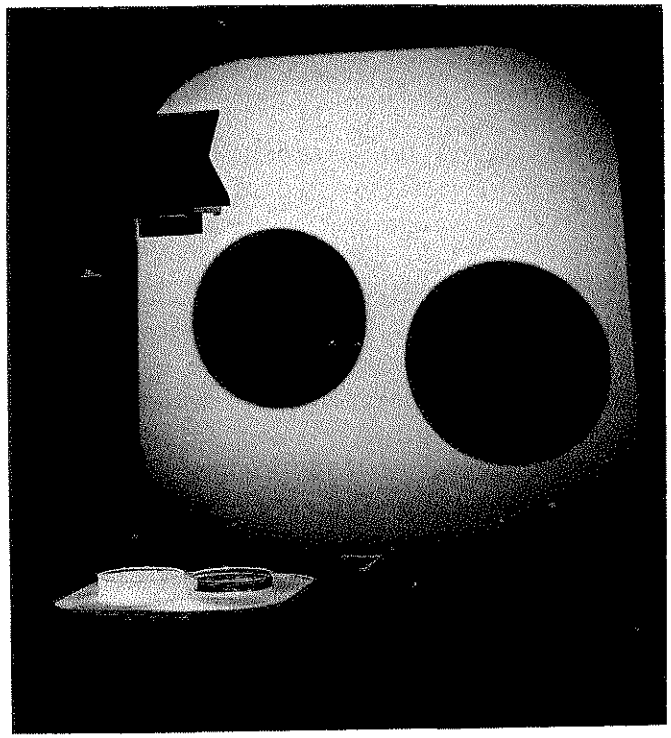

**Figure 5.14** The images of two water filled petri dishes projected on a screen are identical yet their darkness arises from different mechanisms. Light incident on the inky water is attenuated mainly by absorption whereas light incident on the milky water is attenuated mostly by scattering. It is only by looking at the dishes that this difference becomes apparent.

in all directions from the dish. On the other hand, $\tilde{\omega}_o \approx 0$ for inky water as little light is scattered and most of the extinction occurs through absorption. We will see how the parameter $\tilde{\omega}_o$ is fundamental to problems of multiple scattering and, for example, to the remote sensing of clouds from measurements of reflected sunlight.

### 5.3.1 Efficiency Factors and Cross–Sectional Areas

Particle extinction is conveniently defined in terms of a quantity called the *extinction efficiency* $Q_{ext}$. One way of visualizing this quantity is to consider radiation as a stream of photons that flow into a volume containing the scattering particles. Each particle within the



volume blocks a certain amount of radiation resulting in a reduction of the amount of radiation directly transmitted through the volume. The reader must be cautioned at this point as this is not an entirely correct depiction of how extinction takes place. For now, though, this simple view of extinction is a convenient visualization of particle extinction.

The extinction of light as it traverses a volume of spheres can be expressed in terms of a cross–sectional area $C_{ext}$ which is generally different from the geometric cross–sectional area of the particle. For spherical particles of radius $r$, the definition of $Q_{ext}$ then follows as

$$Q_{ext} = \frac{C_{ext}}{\pi r^2} \tag{5.20}$$

When $C_{ext}$ exceeds the value of the geometrical cross–sectional area of the particle, $Q_{ext} > 1$ and more radiation is attenuated by the particle than is actually intercepted by its physical cross–sectional area. Since this extinction occurs by absorption or by scattering or by a combination of both, it follows that

$$Q_{ext} = Q_{abs} + Q_{sca} \tag{5.21}$$

Given the discussion so far, we expect that $Q_{ext}$ depends on the refractive index of the material, the wavelength of radiation, and the size and shape of the particle. Figure 5.15 highlights some of these dependences in the form of a plot of $Q_{ext}$, calculated from Lorenz–Mie theory, as a function of the size parameter $x$ for a water sphere illuminated by light of a wavelength of 0.5 $\mu$m. Somewhat obvious are the large maxima and minima with a superposition of finer scale variations (referred to as ripples). Another familiar phenomenon that may be deduced from Fig. 5.15 is the *reddening* of white light as it passes through a collection of small particles. For fixed refractive index, reddening is depicted by the rapid rise in extinction as $x$ increases from near zero as the wavelength of the radiation decreases and is a general characteristic of nonabsorbing particles smaller than the incident wavelength. For this case, blue light is extinguished (scattered) more than red light, leaving the transmitted light reddened in comparison to the incident light. This reddening is a phenomenon that is not limited to sunlight in the Earth's atmosphere. Interstellar dust particles also redden starlight transmitted through a cloud of such particles. Extinction is obviously highly dependent on the size of the particle.

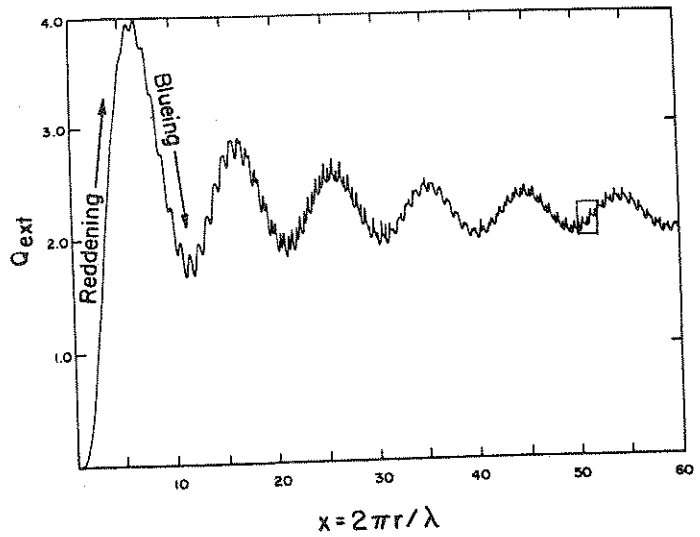


**Figure 5.15** Extinction efficiency for water droplet in air calculated for $\lambda$ =0.5 $\mu$m as a function of size parameter $x$. There are two ways of presenting results of this type. For the example shown, the size parameter varies because particle size varies and the wavelength is kept fixed. The size parameter can also be varied by changing the wavelength while fixing the size of the particle. The results are not the same because as wavelength varies so does the refractive index, and extinction depends not only on the size parameter but also on the refractive index (adapted from Bohren and Huffman, 1983).

### 5.3.2 Extinction by a Cloud of Many Particles

The opposite spectral effect of reddening is the *blueing* of transmitted white light. This occurs when the extinction decreases with increasing $x$ on the high $x$ side of the extinction peaks shown in Fig. 5.15. Unlike reddening, this blueing phenomenon is highly dependent on the character of the particle size distribution and occurs rarely: "once in a blue moon." In fact, this extinction feature and others that depend on particle size are obscured, if not totally obliterated, when the extinction is determined from observations of light scattered by a small volume of air containing particles of a variety of sizes. Under atmospheric conditions, the intensity of radiation scattered by such a volume of particles may be simply obtained as the



addition of the intensities of light scattered by individual particles. Particles in the atmosphere are typically separated by a distance that is much larger than the size of the particle[3] and it can be assumed that there is no correlation between the scattered waves (i.e., phase shifts are randomly distributed and change rapidly so that interference between the light scattered by different particles does not occur).

In Chapter 1, we introduced a convenient mathematical expression for a particle size distribution which we write in the form

$$n(r) = \text{constant}\ \ r^{(1-3b)/b} e^{-r/ab} \tag{5.22}$$

where $n(r)$ is the number of particles per unit volume with a size that falls in the radius range $r$ to $r + dr$ ($n(r)dr$ has units of the inverse of volume) and the parameter $b$ defines the variance of the distribution. Figure 5.16 shows the effect of increasing $b$ on the extinction of the polydispersion determined from a series of Lorenz–Mie calculations. This extinction efficiency is defined as the ratio $\bar{Q}_{ext} = \int_0^\infty n(r) Q_{ext}(r) dr / N_o$ where $N_o$ is the total particle concentration per unit volume. The very fine ripple structure in extinction for the monodispersed cloud (i.e., $b = 0$) disappears as $b$ is systematically increased from zero and the interference structure (i.e., the broad maxima and minima) eventually fades away as the distribution widens. The only remaining features for the widest distributions chosen in this illustration ($b = 0.5$) are reddening at small size parameters and the asymptotic approach to the limiting value 2. The pertinence of both limits to the remote sensing of clouds is discussed shortly.

A dramatic example of the smearing of the interference patterns caused by the superposition of the scattering by different particle sizes is given in Fig. 5.17 which is taken from the work of Roth et al. (1991). In that study, the angular scattering pattern produced by droplets in the path of a laser is recorded by a charged coupled array device. The upper panel of Fig. 5.17 is the intensity distribution produced by a single droplet where the incident beam comes from the right hand side of the diagram and hits the drop in the

[3] The actual volume of air that is typically occupied by cloud droplets is estimated as $V = N_o \frac{4}{3}\pi r^3$ where $N_o$ is the number of droplets per unit volume of air and $r$ is the radius of the spherical droplet. Using the values of $N_o = 10^6$ droplets cm$^{-3}$ and $r$ =10$\mu$m, which is typical of water clouds, $V \sim 10^{-7}$.

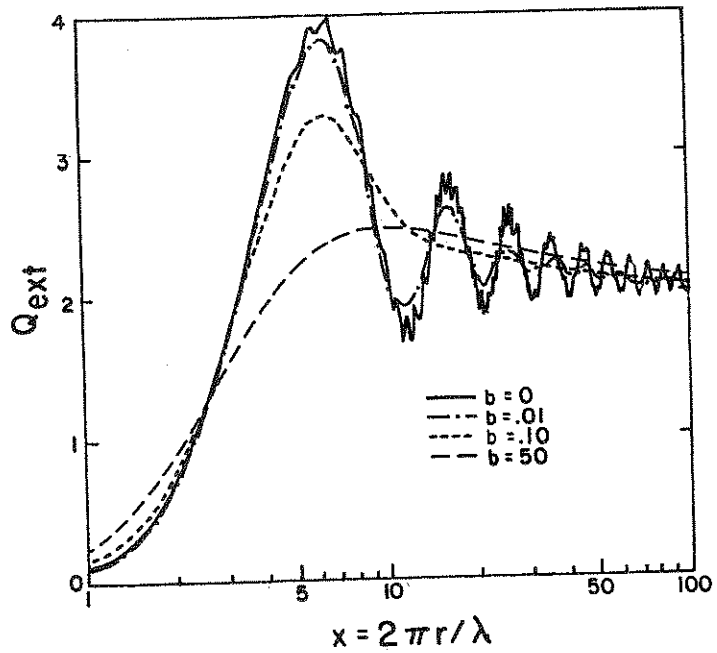


**Figure 5.16** The extinction efficiency, $\bar{Q}_{ext}$, as a function of the effective size parameter $x = 2\pi a/\lambda$ for the values of effective variance $b$ given. Mie theory was used with a refractive index $n = 1.33, \kappa = 0$ (after Hansen and Travis, 1974).

position indicated by the white spot. Light is primarily scattered in the forward direction and many fringes are observed between $\Theta = 0°$ and 180°. We deduce that the size parameter relevant to the experiment shown is large. Rainbows are also visible on the right–hand side of the photograph which represents the backward hemisphere. The lower panel shows what happens to the scattered light when scattering patterns by different sized droplets are superimposed on one another. This superposition smears the fringe pattern of single droplets leaving only the rainbows, the enhanced forward scattering and some slight brightening in the backward direction. Parameters that contain the smearing effect of the size distribution are the volume coefficients for extinction, scattering, and absorption defined as

$$\sigma_{ext,sca,abs} = \int_0^\infty \pi r^2 n(r)\, Q_{ext,sca,abs}\, dr \qquad (5.23)$$



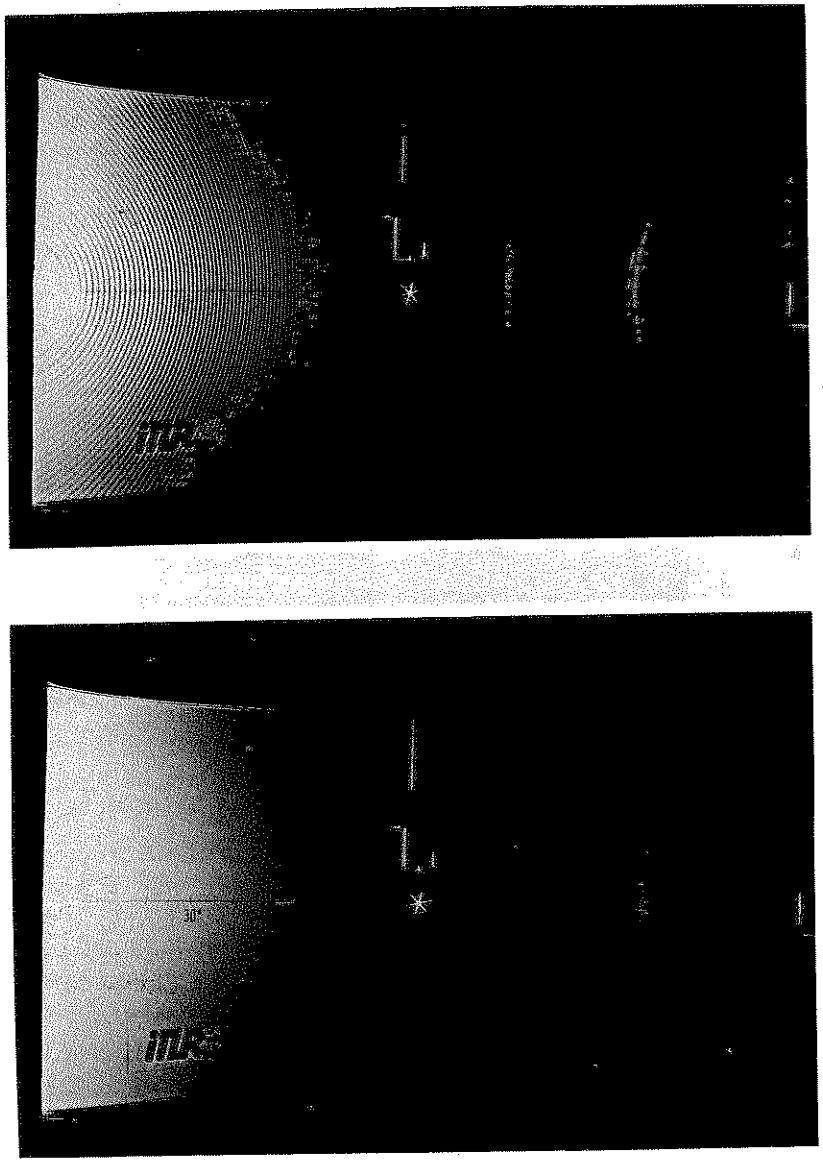

**Figure 5.17** (a) The intensity field of light scattered by droplets of a single size with a size parameter $\approx 250$ (upper panel). The laser enters from the right and the white spots marks the position of the drop. (b) The superposition of the scattered intensity by droplets of different sizes (from Roth et al., 1991).

### 5.3.3 The Rayleigh Limit and Its Application to Cloud Liquid Water Retrieval

The reddening of white light by the scattering of small particles is one of the observable consequences of Rayleigh scattering. In fact, the term Rayleigh scattering tends to be used to refer to extinction by all particles that are much smaller than the incident wavelength even though such terminology lacks historical accuracy. Nevertheless, we adopt this loose terminology in reference to extinction as $x \rightarrow 0$. In this limit, the efficiency factors for absorption and scattering are shown to be (van de Hulst, 1957)

$$\begin{aligned} Q_{abs} &\approx -4x\Im m\left[\frac{\mathrm{m}^2-1}{\mathrm{m}^2+2}\right] \\ Q_{sca} &\approx \frac{8}{3}x^4 \mid \frac{\mathrm{m}^2-1}{\mathrm{m}^2+2} \mid^2 \end{aligned} \tag{5.24}$$

and from these expressions we deduce that $Q_{abs}$ is directly proportional to particle radius (through $x$) whereas $Q_{sca}$ varies as the fourth power of particle radius. Since $x \ll 1$ in the Rayleigh limit, it generally follows that $Q_{abs} > Q_{sca}$ for m complex.

The retrieval of cloud water from measurements of microwave emission exploits this particular property of particle extinction (Chapter 7). The physical basis for these methods is as follows. Scattering by the small cloud droplets (remember these droplets are a few microns in size compared to wavelengths of, say, a few centimeters) is negligible compared to absorption. Substitution of (5.24) into (5.23) produces

$$\sigma_{ext} \approx \sigma_{abs} \approx \frac{-8\pi}{\lambda}\Im m\left[\frac{\mathrm{m}^2-1}{\mathrm{m}^2+2}\right]\int_0^\infty n\,(r)\,\pi r^3 dr \tag{5.25}$$

Therefore the volume extinction coefficient is a function of the cloud liquid water content,

$$\ell = \frac{4\pi\rho_L}{3}\int_0^\infty n(r)r^3 dr$$

where $\rho_L$ is the density of water and the optical depth of the cloud is

$$\tau = \int_{\Delta z}\sigma_{abs}dz = \frac{-6\pi}{\lambda\rho_L}\Im m\left[\frac{\mathrm{m}^2-1}{\mathrm{m}^2+2}\right]\int_{\Delta z}\ell dz \tag{5.26}$$



where the latter integral is the liquid water path ($W$) of the cloud. Given that we know the composition of the cloud particles and thus their refractive index and density $\rho_L$, and given that we know the relationship of the radiation emitted by clouds to the optical thickness (this is discussed in more detail in chapter 7), then the vertically integrated liquid water path can be determined without prior knowledge of the cloud droplet size distribution.

### 5.3.4 The Large Particle Limit and the Extinction Paradox

Another important feature of the $Q_{ext} - x$ spectrum is the tendency for the extinction $Q_{ext}$ either to oscillate around the value of 2 as $x \rightarrow \infty$ as illustrated in Fig. 5.15 or to converge to the value of 2 as in the cases of Fig. 5.16. This behavior is referred to as the *extinction paradox*. Why is it a paradox? Intuition suggests that if we consider extinction as just the radiation that is blocked by the particle, then the extinction cross–section is just the shadow projected by the very large particle. This geometrical view of extinction implies that the limiting value of $Q_{ext}$ is 1 and not 2. However, no matter how large the particle, it still has an edge, and in the vicinity of the edge rays do not behave according to simple geometrical arguments. The energy removed from the forward direction can be thought of as being made up of a part that represents the amount blocked by the cross–sectional area of the particle and another part that is diffracted around the particle's edge.

The diffracted amount eventually fills in the shadow area when viewed far enough from the particle. The total amount removed from the incident beam by diffraction is therefore also characterized by the particle cross–sectional area. The net result is that an amount twice the cross–sectional area of the particle is scattered out of the incident beam. The important point we learn from both this, and from further discussion later, is that particle extinction is both a process of blocking of light as well as actually a result of more subtle interference effects.

Figure 5.18 offers a graphic example of the extinction paradox and emphasizes how diffraction fills in the shadow area with light. This diagram shows the diffraction pattern observed when a small spherical ball bearing is placed between the telescope and a light source that is far removed from the ball. The bright spot in the middle of the pattern is referred to as the *Poisson spot* and shows how

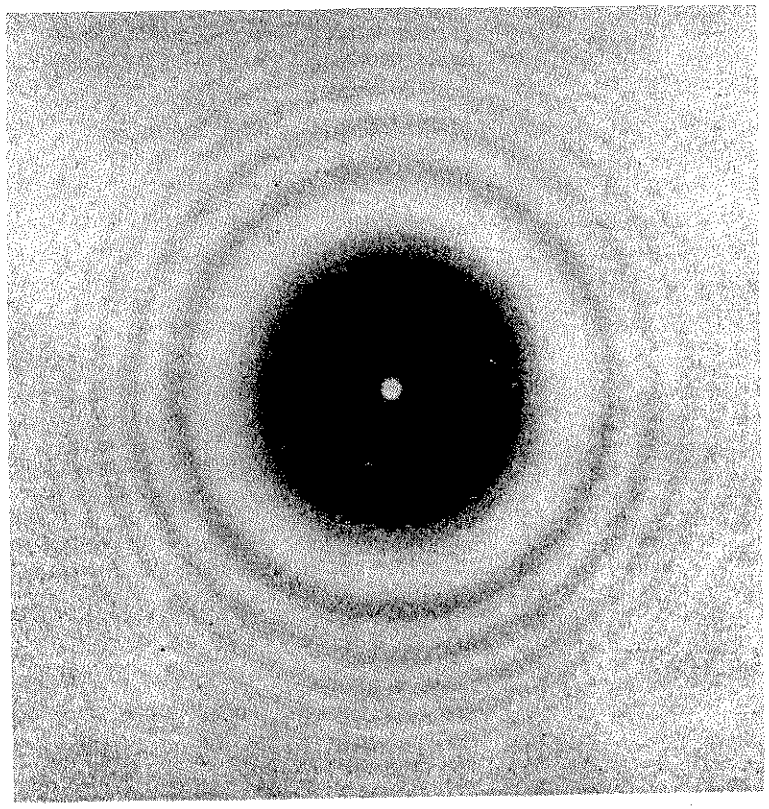

**Figure 5.18** Illustration of the extinction paradox showing the diffraction pattern created when observing a light source obscured at some distance away by a ball bearing of 10mm diameter.

the light is diffracted into the shadow area of the particle, ultimately filling this area.

An important consequence of the large particle extinction limit is that optical thicknesses of many clouds at solar wavelengths are related directly to the vertically integrated liquid water path in a manner analogous to extinction of microwave radiation by cloud droplets. The optical thickness is

$$\tau = \int_{\Delta z} \sigma_{ext} dz \tag{5.27}$$

For wavelengths corresponding to $x \gg 1$ (this occurs when submicron wavelength solar radiation is scattered by cloud particles a few microns in size), we then invoke the asymptotic limit $Q_{ext} = 2$ so



that

$$\tau \approx 2 \int_{\Delta z} [\int_0^\infty n(r) \pi r^2 dr] dz \tag{5.28}$$

Using the definition of the effective radius (see Section 1.6), and the cloud liquid water content $\ell$, the optical thickness then becomes

$$\tau \approx \frac{3}{2\rho_L} \int_{\Delta z} \frac{\ell}{r_e} dz$$

Suppose that $r_e$ does not vary significantly throughout the depth of the cloud, then $\tau$ simplifies to

$$\tau \approx \frac{3W}{2\rho_L r_e} \tag{5.29}$$

This is a relationship that seems to apply for clouds illuminated by visible and near-infrared radiation. Unlike the case for microwave radiation, the optical thickness predicted by (5.29) depends on particle size. Attempts have been made to use measurements of the spectral reflection of solar radiation by clouds, together with some a priori relationship between optical thickness and reflectance, to obtain estimates of both $W$ and $r_e$. These methods are examined in further detail in Chapter 6.

## *Excursus: Ship Tracks*

Concentrations of cloud droplets are determined, to a large extent, by the concentration of cloud condensation nuclei (CCN) in air. Anthropogenic sources of pollution affect these nuclei concentrations. It has been proposed that the climatic impact of pollution might be amplified through its effect on CCNs which in turn alters the cloud droplet concentrations and subsequently alters the cloud albedo. A unique opportunity for testing this hypothesis is provided in the example of ship tracks observed in satellite visible imagery. Under certain conditions, ships influence the structure of shallow cloud layers and the reflection properties of these clouds. Radke et al. (1989) report aircraft measurements of cloud droplet concentrations and other microphysical properties in low level water clouds which are affected by ship stack effluents. An example of data collected during one aircraft flight is shown in Fig. 5.19. These are data on the droplet concentration, liquid water content, interstitial aerosol particle concentration, and radiative fluxes along the flight track. A

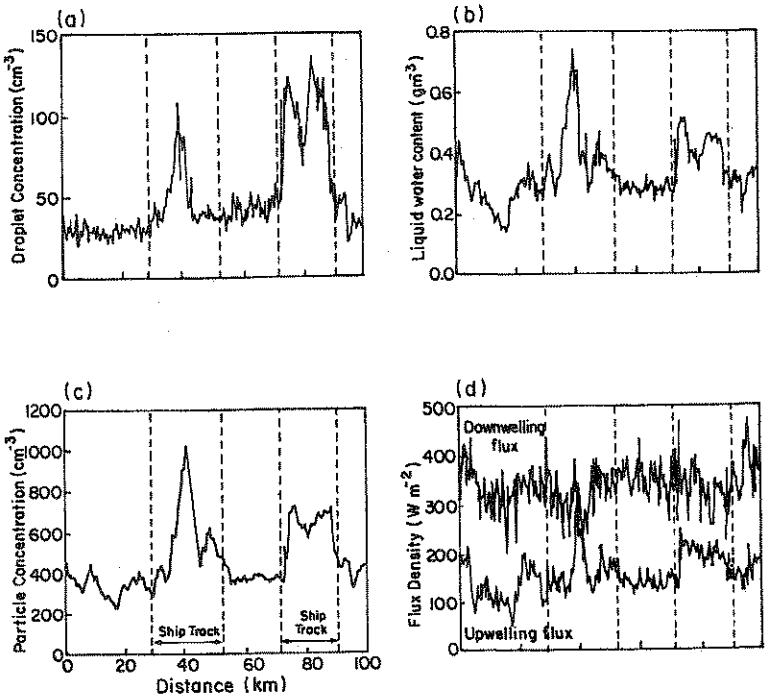


**Figure 5.19** Aircraft transects through two ship tracks showing changes in (a) total droplet concentrations, (b) the liquid water content, (c) total concentrations of cloud interstitial particles, and (d) measured radiation fluxes (from Radke et al., 1989).

key feature is the increased droplet concentration and liquid water content in the vicinity of the ship tracks which combine to increase the optical depth of the cloud and thus its albedo.

We can make some estimate of the effects of the observed increases of droplet concentrations and liquid water content on the optical thickness of clouds by considering the following definitions

$$\ell = \frac{4\pi}{3}\rho_L \int_0^\infty n(r) r^3 dr$$

$$N_o = \int_0^\infty n(r) dr$$



and

$$\bar{r} = \int_0^\infty n(r) r dr / N_o$$

for the liquid water content, total droplet concentration, and mean radius, respectively. Suppose that

$$\ell \approx \frac{4\pi}{3}\rho_L N_o \bar{r}^3$$

then it follows that

$$\bar{r} \approx \left(\frac{3\ell}{4\pi N_o \rho_L}\right)^{1/3}$$

From the definition of optical depth,

$$\tau = \int_{\Delta z} dz \int_0^\infty n(r)\pi r^2 Q_{ext} dr$$

it follows that

$$\tau \approx h 2\pi N_o \bar{r}^2 \approx \text{constant} \times h N_o^{1/3} \ell^{2/3}$$

where we make use of the large particle limit to $Q_{ext}$ and assume the cloud is vertically homogeneous with a geometric depth $h$. The ratio of the cloud optical depths in the ship tracks to those in the unperturbed cloud may be approximated by

$$\left(\frac{\tau_{st}}{\tau_{cl}}\right) \approx \left(\frac{N_{o,st}}{N_{o,cl}}\right)^{1/3} \left(\frac{\ell_{st}}{\ell_{cl}}\right)^{2/3}$$

assuming all other factors being equal. If we take values of the ratios of droplet concentrations and liquid water contents from Fig. 5.19 to be 2 and 1.5, respectively, then the ratio of optical depths is 1.65. This increase in the optical depth of clouds in the vicinity of ship tracks is approximately equally governed by the increase in $N_o$ and the increase in $\ell$.

## 5.4 Scattering Functions

The discussions so far focus on the importance of the attenuation of radiation along the forward direction of propagation. We note in reference to Fig. 5.9, however, that radiation is scattered in all directions although in unequal proportions and in a way that depends on

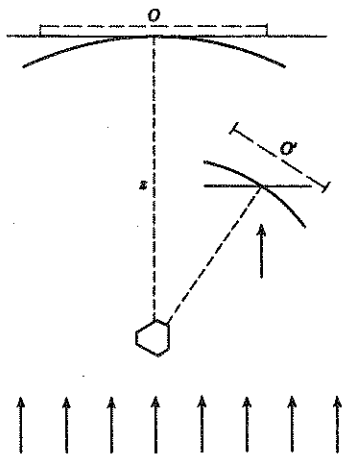


**Figure 5.20** An arbitrary particle that scatters a plane wave to the point $O'$.

particle size, shape, and composition. Many remote sensing methods actually exploit the radiation scattered in directions other than at $\Theta = 0°$. Active sensing by radar and lidar, for instance, makes extensive use of scattering in the backward direction $\Theta = 180°$. A number of passive methods also make use of scattering of radiation by the atmosphere away from the forward direction to derive information about the atmosphere. Thus a mathematical expression for the angular scattering pattern is needed.

### 5.4.1 Amplitude Functions

The scattering pattern is described in terms of a quantity referred to as the *amplitude function* $S(\Theta)$. This may be introduced via the following experiment. A particle of arbitrary shape is illuminated by a plane wave traveling from the negative $z$ direction as shown in Fig. 5.20 and has the form

$$\mathcal{E}_{inc} = \mathcal{E}_o e^{-ikz+i\omega t} \tag{5.30}$$

The scattered wave in the distant field at the point $O'$ is a spherical wave with an amplitude inversely proportional to the distance $R$ from the particle to the observer (Section 2.2) and directly proportional to the incident amplitude. Thus we can write this wave in the



form[4]

$$\mathcal{E}_{sca} = S(\Theta)\frac{e^{-ikR+i\omega t}}{kR}\mathcal{E}_o \tag{5.31}$$

which defines the amplitude function $S(\Theta)$ which is introduced here to describe the scattering pattern as a function of scattering angle. Combining (5.30) and (5.31) yields

$$\mathcal{E}_{sca} = S(\Theta)\frac{e^{-ikR+ikz}}{kR}\mathcal{E}_{inc} \tag{5.32}$$

and in terms of intensities it follows that

$$I_{sca} = \frac{|\,S(\Theta)\,|^2\, I_o}{k^2R^2} \tag{5.33}$$

We discussed earlier how extinction is defined in terms of scattering in the forward direction ($\Theta = 0°$). An important mathematical relationship thus follows from the amplitude function, namely that

$$C_{ext} = \frac{4\pi}{k^2}\Re e[S(0)] \tag{5.34}$$

and this is referred to as the *fundamental extinction formula.*

A more complete treatment of the effects of scattering requires a proper treatment of polarization and this requires four amplitude functions which define an amplitude matrix $\mathbf{S}(\Theta)$ under the linear basis

$$\begin{pmatrix} \mathcal{E}_{sca,\ell} \\ \mathcal{E}_{sca,r} \end{pmatrix} = \begin{pmatrix} S_2 & S_3 \\ S_4 & S_1 \end{pmatrix} \frac{e^{-ikr+ikz}}{kr} \begin{pmatrix} \mathcal{E}_{o,\ell} \\ \mathcal{E}_{o,r} \end{pmatrix} \tag{5.35}$$

where the matrix $\begin{pmatrix} S_2 & S_3 \\ S_4 & S_1 \end{pmatrix}$ is known as the *amplitude scattering matrix*, and the unusual, nonsequential numbering of the matrix elements follows established convention. For homogeneous spherical particles, $S_3 = S_4 = 0$.

[4] In the derivation of van de Hulst (1957, p. 29), a complex factor $i$ appears in the denominator for reasons that become evident in his derivation of cross-sectional areas. We will not outline these derivations here and choose to omit this factor from our discussion.

### 5.4.2 The Scattering Phase Functions

It is more usual to describe the angular patterns of scattered light in terms of a quantity known as the *scattering phase function.*[5] We can consider the relation of the phase function to the amplitude function in the following way. Consider an instrument located at the position at $O'$ in Fig. 5.20 and suppose the area of the detector is $dA$ such that the amount of radiation received by it is confined to the set of directions defined by a small solid angle element $d\Omega = dA/R^2$. The detector is moved to all positions around the particle and measurements are made at each position. The integral of these measurements represents the total energy per unit time at a given wavelength scattered by the particle, namely

$$R^2 \int_{\Xi} I_{sca} d\Omega = \frac{I_o}{k^2} \int_{\Xi} | S(\Theta) |^2 \, d\Omega \tag{5.36}$$

where $\Xi$ denotes the entire sphere of directions. This total scattered power can also be defined in terms of the scattering cross sectional area $C_{sca}$,

$$I_o C_{sca} = R^2 \int_{\Xi} I_{sca} d\Omega \tag{5.37}$$

such that

$$C_{sca} = \frac{1}{k^2} \int_{\Xi} | S(\Theta) |^2 \, d\Omega \tag{5.38}$$

At this point, it is convenient to introduce the quantity

$$\frac{1}{4\pi} P(\Theta) = \frac{| S(\Theta) |^2}{k^2 C_{sca}} \tag{5.39}$$

where $P(\Theta)$ is the scattering phase function. This is a unitless quantity that conveniently represents the variation of the scattered intensity as a function of angle. When integrated over solid angle, $P(\Theta)$ obeys the following condition of energy conservation

$$\frac{1}{4\pi} \int_{\Xi} P(\Theta) d\Omega = 1 \tag{5.40}$$

[5] The use of the word phase to name this function has no relation to the phase of the wave but originates from the astronomical literature and refers to lunar phases.



Equation (5.40) states that, in the absence of absorption, the energy scattered in all directions around the particle equals the amount removed from the incident field. An alternative and convenient way to think about the phase function is in terms of probability of scattering such that the quantity $P(\Theta)d\Omega$ is the probability that a photon is scattered between $\Theta$ and $\Theta + d\Theta$ where the scattering angle increment $d\Theta$ determines the solid angle increment $d\Omega$.

In Chapter 2, four Stokes parameters were introduced to describe the polarization of the intensity field. Whereas we characterize the scattering of the electric field in terms of the amplitude matrix and its four elements $S_1, S_2, S_3$, and $S_4$, scattering of intensities is described in terms of a $4 \times 4$ matrix, called the *phase matrix* P. Each of the 16 coefficients are quadratic expressions of the coefficients $S_1, S_2, S_3$, and $S_4$ as explicitly derived by van de Hulst (1957) The phase matrix often assumes the form

$$\mathbf{P}(\Theta) = \frac{1}{k^2 C_{sca}} \begin{pmatrix} S_{11} & S_{12} & 0 & 0 \\ S_{12} & S_{22} & 0 & 0 \\ 0 & 0 & S_{33} & S_{34} \\ 0 & 0 & -S_{34} & S_{44} \end{pmatrix} \tag{5.41}$$

where $S_{11} = 1/2[| S_2 |^2 + | S_1 |^2], S_{12} = 1/2[| S_2 |^2 - | S_1 |^2], S_{33} = 1/2[S_2^* S_1 + S_2 S_1^*]$ and $S_{34} = i/2[S_2^* S_1 - S_2 S_1^*]$. Matrices of this type are valid for spherical particles and also valid for nonspherical particles given certain scenarios of particle symmetry and orientation that are frequently relevant to the atmosphere. We will not discuss these symmetries here in any more detail but note that matrix (5.41) applies for:

1. spherical particles $S_{11} = S_{22}$ and $S_{33} = S_{44}$ and the additional property $S_{12} = 0$ applies for Rayleigh scatterers
2. randomly oriented particles that each possess a plane of symmetry (i.e., oblate raindrops or needlelike ice crystals that are randomly oriented in the horizontal plane)
3. randomly oriented asymmetric particles if half of the particles are mirror images of the others.

For spherical particles, the relationship between incident and scattered Stokes parameters follows from (5.33), (5.39), and (5.41) as

$$\begin{pmatrix} I_{sca} \\ Q_{sca} \\ U_{sca} \\ V_{sca} \end{pmatrix} = \frac{1}{k^2 R^2} \begin{pmatrix} S_{11} & S_{12} & 0 & 0 \\ S_{12} & S_{11} & 0 & 0 \\ 0 & 0 & S_{33} & S_{34} \\ 0 & 0 & -S_{34} & S_{33} \end{pmatrix} \begin{pmatrix} I_o \\ Q_o \\ U_o \\ V_o \end{pmatrix} \tag{5.42}$$

Examples of measured scattering matrix elements are shown in Fig. 5.21a for small spheres and Fig. 5.21b for irregularly shaped quartz particles. The experimental set up involved detection of He–Ne laser light scattered by a small volume of particles as a function of $\Theta$. The solid curves in Fig. 5.21a correspond to Lorenz–Mie calculations assuming a log–normal size distribution with $r_e = 0.75\ \mu$m and a variance of 0.45. The points correspond to the measured phase matrix normalized in such a way that

$$P_{11} = \frac{1}{4\pi} \int \frac{S_{11}}{k^2 C_{sca}} d\Omega = 1$$

Values of $P_{11}$ agree well with theory but the ratios $-P_{12}/P_{11}$, $P_{34}/P_{11}$, and $P_{33}/P_{11}$ exhibit small deviations near $\Theta = 155°$ and toward the forward direction. For spherical particles, the ratio $P_{22}/P_{11}$ should be exactly unity for all $\Theta$ but the results show departures that exceed the estimated experimental error of $\pm 0.05$ for this ratio. These errors are thought to be due to slight effects of multiple scattering within the scattering volume.

Elements of the phase matrices for irregular quartz particles with a distribution characterized by an equivalent volume effective radius of 15 $\mu$m and a dispersion of 0.8 are also shown in Fig. 5.21b as a function of $\Theta$. The angular variation of $P_{11}$ is flatter than that for the spherical droplets of Fig. 5.21a due to the greater width of the quartz distribution and the irregularities in particle shape that wash out distinctive structures in the angular scattering patterns. The ratio $P_{22}/P_{11}$ differs substantially from the example of water spheres as do $P_{34}/P_{11}$ and $P_{44}/P_{11}$ particularly in the back scattering directions $\Theta > 150°$. We will describe how polarization of backscattered radiation is used qualitatively to diagnose irregularities of particle shape in both Section 5.7 and later in Chapter 8.

## *Excursus: A Polynomial Representation of the Phase Function*

A convenient way to represent the scattering phase function for radiative transfer applications is to express it as a polynomial in scattering angle. The following polynomial series,

$$P(\cos\Theta) = \sum_{\ell=0}^{N} \chi_\ell P_\ell(\cos\Theta) \qquad (5.43)$$



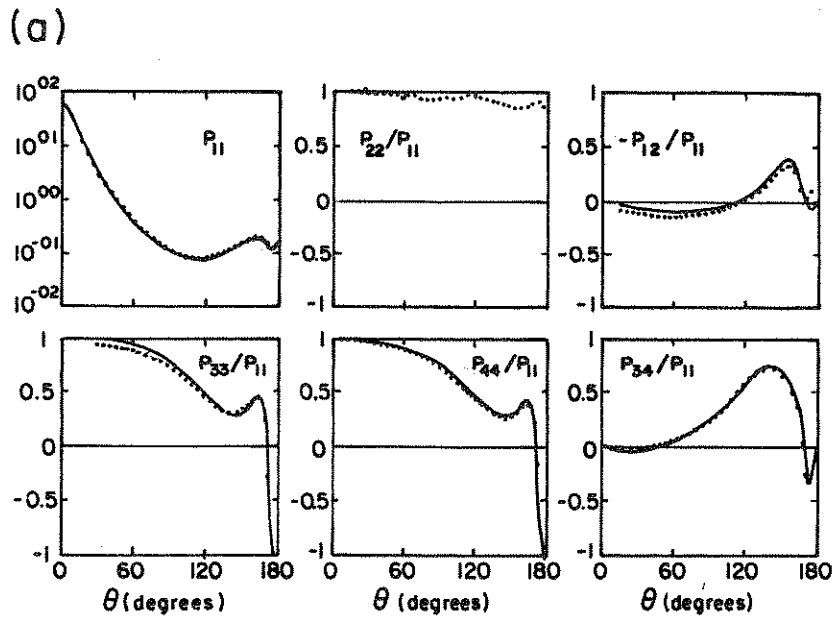


**Figure 5.21** (a) Six scattering matrix elements of an ensemble of water droplets as a function of scattering angle. Measurements are denoted by symbols and the solid curve is from Lorenz–Mie theory. The wavelength is 632.8 nm and the refractive index m=1.332 (after Kuik et al., 1991).

is most commonly used since it has special advantages when applied to radiative transfer, but these need not concern us here. In this series, $P_\ell$ is the $\ell$th order Legendre polynomial and $\chi_\ell$ are the associated expansion coefficients, defined as

$$\chi_\ell = \frac{(2\ell+1)}{2} \int_{-1}^{1} P(\cos\Theta) P_\ell(\cos\Theta) d\cos\Theta \qquad (5.44)$$

A general guideline is that the larger the particle, and hence the more forward the scattering, the more polynomial terms are required to represent the true phase function. Simpler, analytic functions require fewer polynomial terms. Table 5.1 presents a few phase functions commonly encountered in different scattering problems, together with their first four expansion coefficients.

(b)

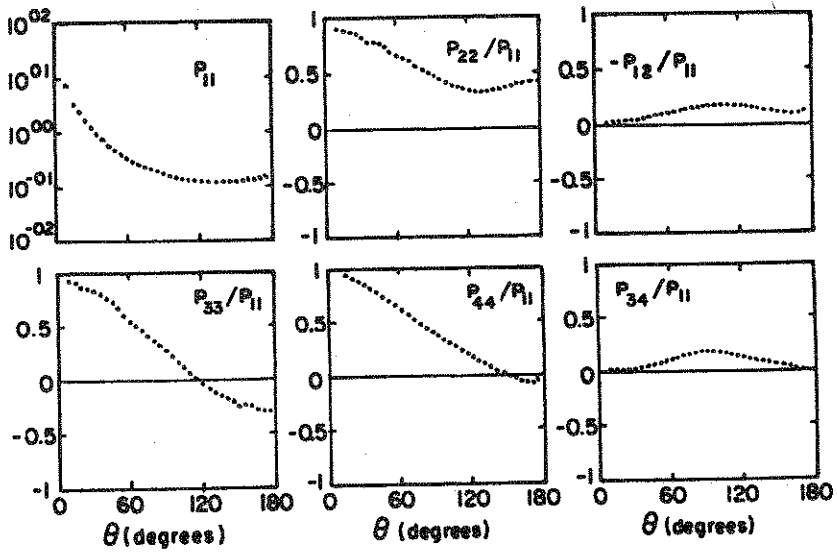


**Figure 5.21** (Cont.) (b) Six scattering matrix elements of an ensemble of randomly oriented irregularly shaped quartz particles as a function of scattering angle (after Kuik et al, 1991).

The expansion coefficients for the two analytic functions given in Table 5.1 are expressed in terms of the *asymmetry parameter* $g$. This is a parameter of some importance to particle scattering problems and is defined as

$$g = \frac{1}{3}\chi_1 \tag{5.45}$$

An interpretation of this parameter is:
- $g = 1$ for complete forward scattering.
- $g = -1$ for complete backward scattering.
- $g = 0$ for isotropic or symmetric scattering (e.g., Rayleigh scattering).

For solar wavelengths and water droplet clouds, $g$ is quasi–constant with an approximate value 0.85. Values of this parameter for irregular particles, like ice crystals, at solar wavelengths are not well known, but they are thought to be significantly different from the values associated with spherical particles.



**Table 5.1** Legendre coefficients of selected phase functions

| Scatter type | Formula for $P(\Theta)$ | Legendre Coefficients | | | |
|---|---|---|---|---|---|
| | | $\chi_0$ | $\chi_1$ | $\chi_2$ | $g$ |
| Isotropic | 1 | 1 | 0 | 0 | 0 |
| Rayleigh | $\frac{3}{4}(1+\cos^2\Theta)$ | 1 | 0 | $\frac{1}{2}$ | 0 |
| Henyey–Greenstein | $\frac{1-g^2}{(1+g^2-2g\cos\Theta)^{3/2}}$ | 1 | $3g$ | $5g^2$ | $g$ |
| Forward† plus backward | $(1+g)\delta^+ +(1-g)\delta^-$ | 1 | $3g$ | $5g^2$ | $g$ |

†$\delta^+ = 1$ when $\theta = 0°$ and zero otherwise. Similarly, $\delta^- = 1$ when $\theta = 180°$ and zero otherwise; $g$ is the asymmetry parameter.

### 5.4.3 An Example of the Remote Sensing of Ice Crystal Phase Functions

A method for measuring the scattering phase function for nonspherical ice particles was introduced by Platt and Dilley (1984). The technique involves the measurement of solar radiation transmitted through the cloud (Fig. 5.22a) and collected by a receiver at the ground. Monitoring this radiation throughout the day as the sun passes across the sky provides a way of determining the scattering phase function for different values of the scattering angle. A number of assumptions are necessary for the analysis scheme of Platt and Dilley to work. The cloud must exist in a quasi–steady state so that the ice crystal properties remain unchanged with time. The cloud must also be spatially homogeneous so as not to change as it advects over the receiver. The cloud must also be optically thin so that smearing effects of multiple scattering are minimized. These conditions rarely apply in the real atmosphere, but they supposedly existed during the experiment reported by Platt and Dilley.

For the experimental configuration given in Fig. 5.22a, the energy $E$ per unit area and per unit time received at the detector which

has a field of view $\Delta\Omega$, and a spectral bandwidth $\Delta\lambda$, is

$$E \approx E_d + E_s + E_a \approx (I_d + I_s + I_a)\Delta\Omega\Delta\lambda \qquad (5.46)$$

where $I_d$ is the intensity due to scattering of the direct solar radiation by clouds, $I_s$ is the component of solar radiation reflected upwards from the surface and back to the receiver from the cloud, and $I_a$ is the solar radiation scattered by the atmosphere below the cloud into the receiver. The amount of solar radiation, inclined at an angle $\theta_o$ from the vertical, that reaches some level in the cloud is $F_o \exp(-\tau/\mu_o)$ where $\mu_o = \cos\theta_o$ (see Chapter 6 for further discussion and the derivation of this expression). The rate of change of $I_d$ with $\tau$ then follows from radiative transfer theory (Section 6.3),

$$\frac{dI_d}{d\tau} = -F_o \exp(-\tau/\mu_o) P(\Theta)/4\pi \qquad (5.47)$$

where $\Theta$ is the scattering angle. The intensity at some level corresponding to $\tau^*$ is

$$I_d(\tau^*) = F_o \frac{P(\Theta)}{4\pi} \mu_o [1 - \exp(-\tau^*/\mu_o)] \qquad (5.48)$$

which specifies the intensity of sunlight scattered from cloud base toward the receiver along the scattering angle $\Theta$ in terms of $\tau^*$, the optical depth of the cloud. According to (5.46), the energy received at the detector due to the scattering of direct sunlight is

$$E_d = I_d \Delta\Omega\Delta\lambda = F_o \frac{P(\Theta)}{4\pi} \mu_o [1 - \exp(-\tau^*/\mu_o)] \mathcal{T}_a \Delta\Omega\Delta\lambda \qquad (5.49)$$

where $\mathcal{T}_a$ is the transmission function for the atmosphere below the cloud.

The phase function follows if experimentally derived values of all other factors in (5.49), together with estimates of the remaining two contribution terms of (5.46), are determined. The interested reader can refer to the reference for a discussion of how these different factors were estimated. Values of $P(\Theta)/4\pi$ retrieved from (5.49) are shown in Fig 5.22b as a function of scattering angle. The theoretical reference curve shown on this diagram applies to a hexagonal columnar crystal $30\mu m$ wide and $120\mu m$ long, based on the ray tracing calculations of Wendling et al. (1982). Certain remarkable



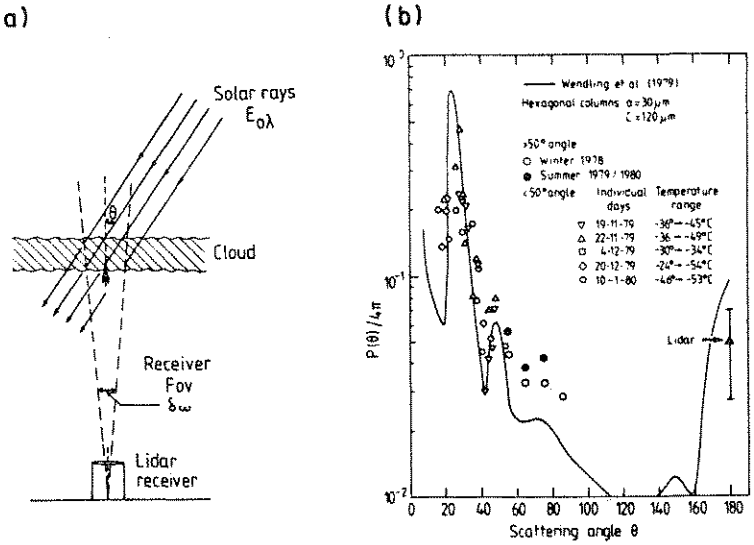


**Figure 5.22** (a) The geometric configuration of the Platt and Dilley experiment. (b) The retrieved, normalized scattering phase function at various scattering angles compared to a theoretical curve for hexagonal ice crystals (from Platt and Dilley, 1984).

features appear in the retrieved phase function that match the theoretical curve for hexagonal columns, including the 22 degree and 46 degree haloes. There is also a suggestion that the actual scattering differs from the theoretical scattering curve in the range $\Theta > 60°$.

## 5.5 A Simple Diffraction Theory of Particle Extinction

The earlier remark that extinction arises more from interference than from a blocking of the incident wave is the basis for an approximate theory for particle extinction and absorption. This approximate theory owes its origins to van de Hulst (1957) and is known as the ***anomalous diffraction theory*** (ADT). One of the major virtues of this theory, and one exploited in different remote sensing problems, is the inherent simplicity of its mathematical form.

The anomalous diffraction theory models forward scattering in the following way. Consider a plane wave[6] that passes through a

[6] We consider a spherical particle here only for simplicity. The ideas described apply to any shape of particle and the approach requires only the specification of the path length of a ray within the particle.

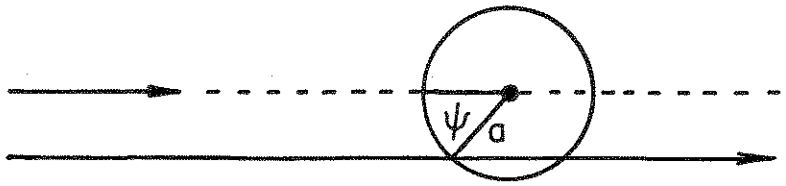


**Figure 5.23** ADT geometry for a spherical particle of radius $a$.

spherical particle of radius $r$. Extinction can be defined in terms of the characteristics of the wave projected on a reference screen some distance from the particle. The geometry relevant to this discussion is given in Fig. 5.23. Two basic assumptions are now introduced:

- The particle is assumed to be large relative to the wavelength of the wave such that $x \gg 1$. Under these circumstances, we can ignore the individual waves within the particle and trace the passage of the wave as a ray.
- The refractive index of the particle is close to that of the background (i.e., m$\approx$ 1) so that a ray passes through the particle without suffering any significant refraction.

The resultant wave on the screen is

$$\mathcal{E}_{res} = \mathcal{E}_{inc} + \mathcal{E}_{sca} \tag{5.50}$$

The ADT supposes that this wave may be expressed entirely in terms of the phase difference between the ray that penetrates the particle to one that is diffracted by the particle's edge. Thus we write

$$\mathcal{E}_{res} = \mathcal{E}_{inc}[1 + e^{-i\Delta\phi}]e^{i\phi_o} \tag{5.51}$$

where from simple geometric considerations the relative phase difference for the ray shown in Fig. 5.23 is

$$\Delta\phi = 2x \sin\psi(\mathrm{m} - 1) = \rho \sin\psi \tag{5.52}$$

where $\rho$ is the relative phase lag experienced by the ray passing along the diameter of the sphere relative to a ray outside the particle and



$\psi$ is the angle defined in Fig. 5.23. Making use of (5.32), we arrive at

$$S(\Theta = 0) = \frac{k^2}{2\pi} \int_G \frac{\mathcal{E}_{sca}}{\mathcal{E}_{inc}} dA \tag{5.53}$$

where the integration is performed over the geometric shadow area $G$ of the particle. Substitution of (5.51) and (5.52) into (5.53) leads to

$$S(\Theta = 0) = x^2 \mathcal{K}(i\rho) \tag{5.54}$$

where

$$\mathcal{K}(w) = \frac{1}{2} + \frac{e^{-w}}{w} + \frac{e^{-w} - 1}{w^2}$$

and thus

$$Q_{ext} = 4\Re\mathrm{e}\{\mathcal{K}(i\rho)\} \tag{5.55}$$

follows from the fundamental extinction formula (5.34).

Figure 5.24, taken from the original work of van de Hulst, compares an example of $Q_{ext} = Q_{sca}$ calculated using this simple formula for extinction with that from Lorenz–Mie theory. The approximate formula clearly has some shortcomings, lacking the very fine structure observed in the Lorenz–Mie theory, but the large maxima and minima of $Q_{ext}$ and the position of these defined relative to the central phase shift $\rho$ are well represented. This simple theory allows us to interpret these pronounced extrema as interference features. The maxima occur when the term $-e^{-i\Delta\phi}$ enhances the term 1 in the integrand of (5.53) from which $Q_{ext}$ was computed. Since one term represents the transmitted light and the other term represents the diffracted light, we can deduce that the maxima are due to favorable interference of the transmitted and diffracted waves and that the minima are a result of unfavorable interference. By plotting $Q_{ext}$ as a function of $\rho$, we are able to present the extinction for different values of m on a common scale.

## *Excursus: Particle Absorption in the ADT Approximation*

The derivation given earlier applies to nonabsorbing particles. For an absorbing particle with $\mathrm{m} = n - i\kappa$, the requirement that $|\,\mathrm{m} - 1\,| \ll 1$ means that both $|\,n - 1\,|$ and $|\,\kappa - 1\,|$ be $\ll 1$. It is also convenient to express the absorption in terms of an angle $\zeta$ such that

$$\tan\zeta = \frac{\kappa}{n - 1} \tag{5.56}$$

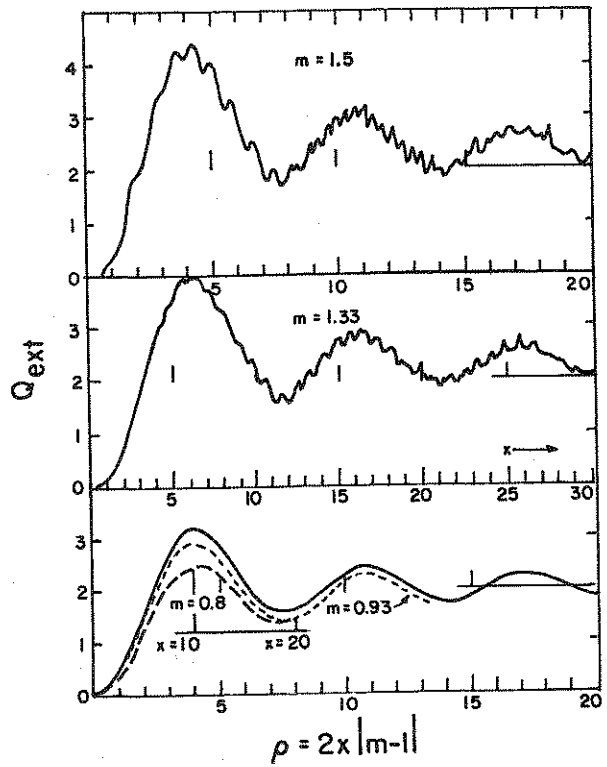


**Figure 5.24** Extinction curves computed from Lorenz–Mie formulas for $m$ =1.5,1.33,0.93,0.8. The abscissa is $\rho = 2x(\mathrm{m}-1)$ and is common to the upper two Lorenz–Mie curves as well as to the bottom ADT curves (van de Hulst, 1957).

assumes values varying from 0 (no absorption) to $\infty$. The real phase shift parameter $\rho = 2x(n-1)$ was introduced earlier. The complex phase shift parameter for a path through the center of the sphere is

$$\rho^* = 2x(\mathrm{m}-1) = \rho(1 - i\tan\zeta)$$

where the real part is the actual phase shift and the imaginary part is associated with the decay of the wave amplitude. The derivation of $Q_{ext}$ and $Q_{abs}$ will not be described further as the interested reader can find these in van de Hulst (1957, Chapter 11, p. 179). The results of the derivations are:

$$Q_{ext} = 4\Re e\{\mathcal{K}(i\rho + \rho\tan\zeta)\} \qquad (5.57a)$$



$$Q_{abs} = 2\mathcal{K}(4v) \qquad (5.57b)$$

where the absorption by the particle is determined as simply the integrated attenuation of all rays that penetrate the particle. In the expression for $Q_{abs}$, $v = 2x\kappa$ and $x = 2\pi a/\lambda$ is the size parameter of a sphere of radius $a$. Bohren and Nevitt (1983) provide a slight improvement to $Q_{abs}$ which is cast in terms of $\mathcal{K}(v)$ by Flatau (1992) as

$$Q_{abs} = c[2\mathcal{K}(4v) - h^2\mathcal{K}(4av)] \qquad (5.58)$$

where

$$h = \frac{(n^2-1)^{1/2}}{n}$$

and

$$c \approx n^2$$

for $n$ close to unity. Equation (5.58) predicts that $Q_{abs}$ increases systematically with increasing $v$ in the manner illustrated by the solid curve in Fig. 5.25. The symbols represent calculations of $Q_{abs}$ obtained from Lorenz–Mie theory and the solid curve is (5.58) derived for a 5 $\mu$m water droplet for wavelengths spanning from 0.7 to 3 $\mu$m. The value of (5.58) is that it shows how the behavior of $Q_{abs}$ uniquely depends on $v$. Two particles of different radius $a$, and composition $\kappa$, absorb the same amount of radiation when the respective values of $v$ match each other.

## 5.6 Scattering by Spheres: A Brief Outline of Lorenz–Mie Theory

The theory for scattering by dielectric spheres was developed independently by Ludwig Lorenz in 1890 and Gustav Mie in 1908 (refer to the discussion of these developments in the bibliographical notes at the end of this chapter). The derivation of the solution is a straight forward application of classical electromagnetic theory and only the resulting formulas are given here. The solutions are expressed as infinite series and the rates of convergence of these series depend on the value of the size parameter $x$. The two scattering amplitude functions have the form

$$S_1(\Theta) = \sum_{n=1}^{\infty} \frac{2n+1}{n(n+1)}[a_n\pi_n(\cos\Theta) + b_n\tau_n(\cos\Theta)]$$

$$S_2(\Theta) = \sum_{n=1}^{\infty} \frac{2n+1}{n(n+1)}[a_n\tau_n(\cos\Theta) + b_n\pi_n(\cos\Theta)] \qquad (5.59)$$

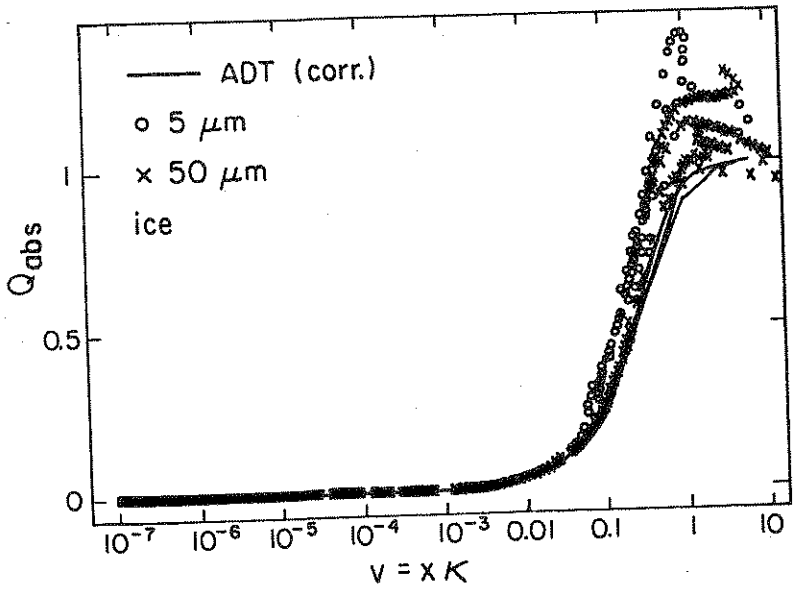


**Fig. 5.25** The absorption efficiencies derived from Lorenz–Mie theory (symbols) and from (5.58) (solid curve) as a function of the absorption similarity parameter $v$.

where

$$\pi_n(\cos\Theta) = \frac{1}{\sin\Theta} P_n^1(\cos\Theta)$$
$$\tau_n(\cos\Theta) = \frac{d}{d\Theta} P_n^1(\cos\Theta) \qquad (5.60)$$

and where $P_n^1$ is the associated Legendre polynomial (e.g., Abromowitz and Stegun 1971). The coefficients $a_n$ and $b_n$ are referred to as Mie scattering coefficients and are functions of refractive index m and size parameter $x$. The mathematical forms of these coefficients are given as ratios of Ricatti–Bessel functions and can be found in the references on Lorenz–Mie scattering cited at the end of this chapter. The extinction and scattering efficiencies are also given by the series

$$Q_{ext} = \frac{2}{x^2} \sum_{n=1}^{\infty} (2n+1)\, Re\,(a_n + b_n) \qquad (5.61a)$$

$$Q_{sca} = \frac{2}{x^2} \sum_{n=1}^{\infty} (2n+1)\,(|\,a_n\,|^2 + |\,b_n\,|^2) \qquad (5.61b)$$



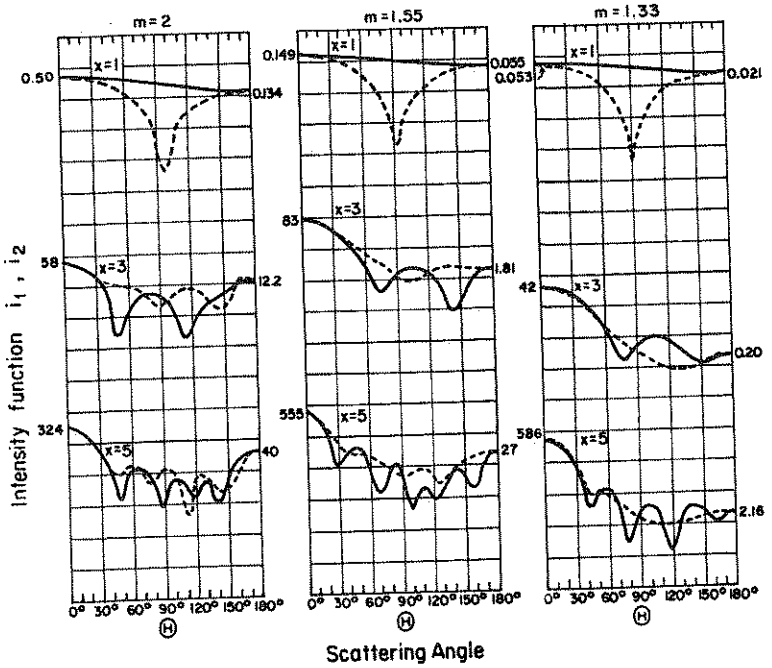


**Figure 5.26** Scattering diagrams derived from Lorenz–Mie theory for a single particle. The solid curves are for $i_1$ and the broken curves are for $i_2$. Numerical values of $i_1$ and $i_2$ are specified at $\Theta = 0$ and 180 degrees (after van de Hulst, 1957).

Example calculations of the intensity functions $i_{1,2} = |\,S_{1,2}\,|^2$ are shown in Fig. 5.26 for a given particle of fixed size. These intensity functions reveal how the number of fringes increases over the range $0^o \leq \Theta \leq 180^o$ as the size parameter increases (compare these to Fig. 5.17). It is also noteworthy how the scattering in the forward direction increases as $x$ increases according to our earlier expectation.

Figure 5.27 presents the scattering phase function $P = \frac{1}{2}(P_1 + P_2)$ for unpolarized radiation[7] versus scattering angle $\Theta$ (upper panels) and the degree of linear polarization (lower panels), defined as

$$LP = \frac{P_1 - P_2}{P_1 + P_2}$$

also plotted as a function of scattering angle. The calculations are shown for m= 1.33 and 1.5 and three size distributions characterized

[7] We use $P_1$ and $P_2$ for $S_{11}/k^2C_{sca}$ and $S_{22}/k^2C_{sca}$, respectively.

by three different values of the effective size parameter $x_m = 2\pi a/\lambda$ where $a$ is the parameter of the size distribution given by (5.22). The scattering phase function becomes more peaked in the forward direction as $x_m$ increases in accordance with our expectations. A sharp increase in scattering also occurs in the backscattering direction ($\Theta = 180^o$) for the large spheres. This strong enhancement, also noted in reference to Fig. 5.17, is a characteristic of spherical particles and is referred to as the *glory*. One of the major contributors to this effect is the tangential ray that just grazes the surface, setting up surface waves that travel around the sphere. The interference of these surface waves with those that penetrate the particle produces this effect. Also noteworthy is the way the polarization patterns alter as $x_m$ changes. A comparison of Fig. 5.27 with Fig. 5.4a illustrates how the magnitude of the maximum degree of polarization is considerably reduced from the value of 100% that we associate with pure Rayleigh scattering at $\Theta = 90^o$.

The formal Lorenz–Mie solution does not, at first sight, seem to offer much in the way of a physically intuitive picture of the mechanism of the scattering process. However, some qualitative insights can be obtained from the theory. We know that the scattered wave arises from oscillations of the electrons in the particle that are excited by the incident wave. Distributions of electric charges may be represented by a superposition of electric multipoles with arbitrary moments located at some origin point. If, as in the case of scattering, the distributions of charges and currents oscillate synchronously with the exciting wave, the scattered radiation arises from the corresponding oscillating multipoles. The oscillating electric multipoles produce partial electric waves and the oscillating magnetic multipoles produce partial magnetic waves. The amplitude and phase of each wavelet associated with a particular electric multipole is given by $a_n$ and $b_n$ is associated with the corresponding magnetic multipole. The electric dipole moment is therefore proportional to $a_1$ and the magnetic dipole moment is proportional to $b_1$ and the higher order $a_n$ and $b_n$ coefficients are each related to corresponding higher order multipole radiation.

An important example of the application of Lorenz–Mie theory in remote sensing is in the interpretation of the polarization of sunlight that results from the reflection by clouds in the atmosphere of Venus. Even up to the 1920s it was debatable whether sunlight reflected by Venus was in fact polarized. However, with the development of precision polarimeters capable of accuracies of about 0.1



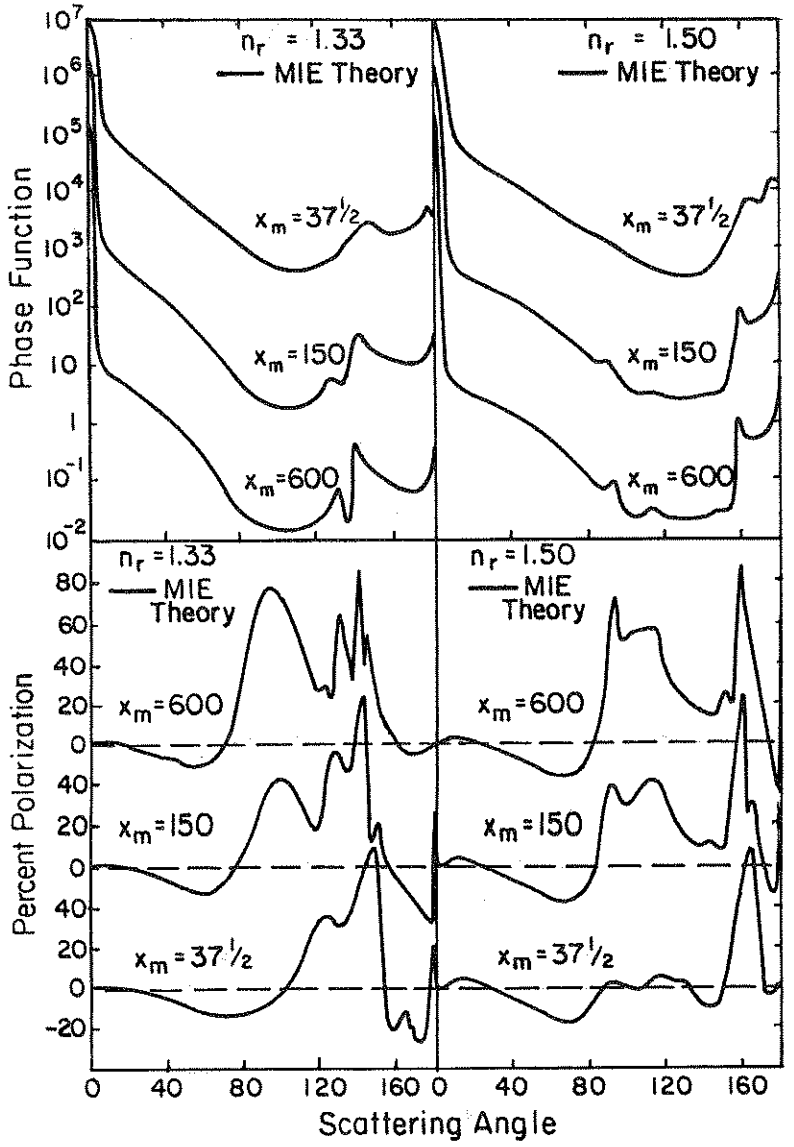


**Figure 5.27** The scattering phase function and degree of polarization calculated from Lorenz–Mie theory as a function of $\Theta$. The results are shown for two real refractive indices and different values of the effective size parameter $x_m$ (adapted from Hansen and Travis, 1974).

%, it was revealed that reflected light from Venus exhibits distinct polarization features. Hansen and Hovenier (1974) used these polarization properties to deduce information about the size of the cloud particles. An example of the measured variation of polarization as a function of phase angle (which is defined as $180° - \Theta$) is presented in Fig. 5.28. The model results of Hansen and Hovenier (1974) are superimposed on these observations. From the comparisons between the calculated reflectivities and observed quantities, Hansen and Houvenier deduced that:

- the cloud particles at cloud top were spherical.
- the effective radius was $\sim 1\mu$m.
- the particle size distribution was very narrow with an effective variance, $b \sim 0.07$.
- the particles were deduced to be sulphate spheres based on the refractive index $n = 1.44$ that provided a match to the observations.

The successful analysis of the polarization of Venutian clouds, however, has not been repeated for terrestrial clouds. The success of this kind of analysis for Venus depends largely on the fact that the cloud particles are spheres. Irregularly shaped ice particles that occur in the upper portions of deep convective clouds or in the cirrus clouds that veil the Earth introduce effects that greatly complicate polarization patterns making unambiguous interpretation of polarization in terms of particle size more difficult.

## 5.7 Particle Backscattering

Understanding which properties of particles govern the amount of radiation that is backscattered from them is crucial to many remote sensing applications and especially to applications involving active sensing. We now discuss particular properties of particle backscattering relevant to both radar and lidar backscattering measurements. It is convenient to introduce the following definitions of cross–sectional areas:

- The differential cross–section

$$C_d(\Theta) = \frac{C_{sca}}{4\pi} P(\Theta) \qquad (5.62a)$$

  where $C_d$ is a measure of the amount of incident radiation scattered into the direction $\Theta$ per unit solid angle.

- Bistatic (radar) cross–section

$$C_{bi} = 4\pi C_d(\Theta) \qquad (5.62b)$$

# Plates

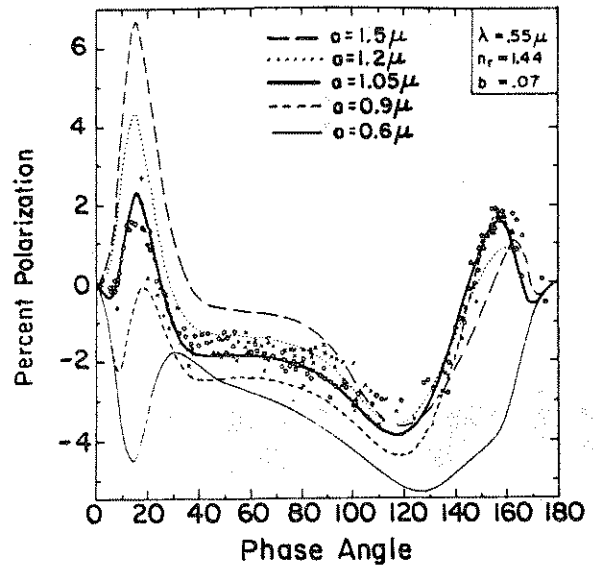


**Figure 5.28** Polarization of Venus. Observational points and calculations centered at $\lambda$ =0.55 $\mu$m. All curves are for spheres with a refractive index of 1.44. The different curves show the effect of different values of $a$ in (5.23). All size distributions assume $b$ =0.07 (after Hansen and Hovenier 1974).

which is the total scattering cross–sectional for a particle that scatters isotropically by an amount $C_d(\Theta)$.

- Backscattering cross–section

$$C_b = 4\pi C_d(\Theta = 180^o) \tag{5.62c}$$

which has a similar interpretation to (5.62b) except that the scattering direction is now specified to be directly opposite the incident direction.

### 5.7.1 Backscattering by Small Spheres

Since scattering by particles is described in its most general form by the phase matrix $\mathbf{P}(\Theta)$, then the scattering cross–sections defined earlier are also matrix quantities as described shortly. For now, however, the much simpler situation of backscattering of unpolarized light by spherical particles is treated. Lorenz–Mie theory provides

us with an expression of $C_b$ for a sphere of radius $r$

$$C_b = \frac{\pi r^2}{x^2} \mid \sum_{n=1}^{\infty} (-1)^n (2n+1)(a_n - b_n) \mid^2 \qquad (5.63)$$

which follows from (5.62c) and (5.59) assuming $\Theta = 180^o$.

When applying (5.63) to radar backscattering problems, it is useful to consider the behavior of $C_b$ in the limit as $x \to 0$. In this limit it is possible to carry out a small argument expansion of the Bessel functions that define these coefficients and express them as polynomials of $x$ (refer to Bohren and Huffman, Chapter 5). If we neglect all terms of higher order than $x^5$, then

$$\begin{aligned} b_1 &\approx -\frac{i}{45}(m^2-1)\,x^5 + O(x^7) \\ a_1 &\approx -\frac{2i}{3}\left(\frac{m^2-1}{m^2+2}\right)x^3\left[1+\frac{3}{5}\left(\frac{m^2-2}{m^2+2}\right)x^2\right] + O(x^6) \\ a_2 &\approx -\frac{i}{15}\left(\frac{m^2-1}{2m^2+3}\right)x^5 + O(x^7) \end{aligned} \qquad (5.64)$$

where all other coefficients $(a_3 \ldots; b_2, b_3, \ldots)$ are neglected. Retaining $x^3$ terms leaves only the first term of $a_1$, the electric dipole term, which then yields on substitution in (5.63)

$$C_b = \frac{\lambda^2}{\pi} x^6 \mid \frac{m^2-1}{m^2+2} \mid^2 = \frac{\pi^5}{\lambda^4} \mid K \mid^2 D^6 \qquad (5.65)$$

where $K$ is used for $(m^2-1)/(m^2+2)$ and $D$ is the particle diameter. The path from Lorenz–Mie theory to (5.65) serves to emphasize how the Rayleigh scattering limit is a special case of Lorenz–Mie scattering.

Figure 5.29a provides an example of particle backscattering calculated using (5.63) as a function of the size parameter. The backscattering is expressed in terms of the *backscattering efficiency* $Q_b = C_b/\pi r^2$ and is shown for water and ice spheres assuming a wavelength of 10 cm which is commonly used by weather radar. Also shown for comparison are the efficiencies derived from Rayleigh scattering using (5.65). We note that the backscattering by water spheres in the range $x < 2$ is considerably larger than backscattering by ice spheres of the same size. As $x$ increases, the comparative roles reverse with backscattering by ice spheres exceeds that of water



spheres. Large water droplets significantly absorb 10 cm radiation, and backscattering is small compared to large ice particles. Figure 5.29b also shows how the Rayleigh approximation to backscattering deviates significantly from the Lorenz–Mie solution as $x$ is increased beyond about $x = 1$.

The range of $x$ over which the Rayleigh approximation applies for wavelengths typical of radars has been examined in detail by several investigators. Figure 5.29b also presents the variation of the ratio $C_{b,L-M}/C_{b,Ray}$ as a function of $x$ for various radar wavelengths. It may be concluded from this diagram that scattering of 3cm wavelength radiation by precipitation drops smaller than about 2mm can be approximated by Rayleigh scattering to within 25% of Lorenz–Mie scattering and that virtually all precipitation, except perhaps hail, may be regarded as Rayleigh scatterers at wavelengths of about 10 cm.

### 5.7.2 Backscattering by Nonspherical Particles

It was mentioned in section 5.3 how scattering, especially in the backward direction, is sensitive to particle shape. Backscattering by irregularly shaped particles is now discussed.

In the most general terms, the scattering matrix introduced in Section 5.5 has 16 independent parameters. For many situations applicable to particles in the atmosphere, the phase matrix has a simpler form like that given by (5.41). We will now consider the backscattering by particles governed by this particular phase matrix. In doing so, we find it convenient to discuss polarization by backscattering in terms of ratio quantities that are used in lidar and radar studies of clouds. These quantities are introduced here to demonstrate their relationship to the scattering phase matrix.

*Lidar Depolarization Ratio*

The depolarization ratio is a quantity often used in lidar studies of particle scattering. It is convenient to think of this lidar parameter in terms of a receiver such as that described in our simple, earlier experiments discussed in Section 2.3. Most lidar systems transmit a laser pulse with a linear polarization, and receive the returned pulse using the optical elements as arranged in Fig. 2.13. We denote the intensity of the returned pulse by $I_\ell$ for the case when the polarizer is aligned along the direction parallel to the polarization of the transmitted pulse. When perpendicular to the polarization direction of this transmission, the detected intensity on transmission through

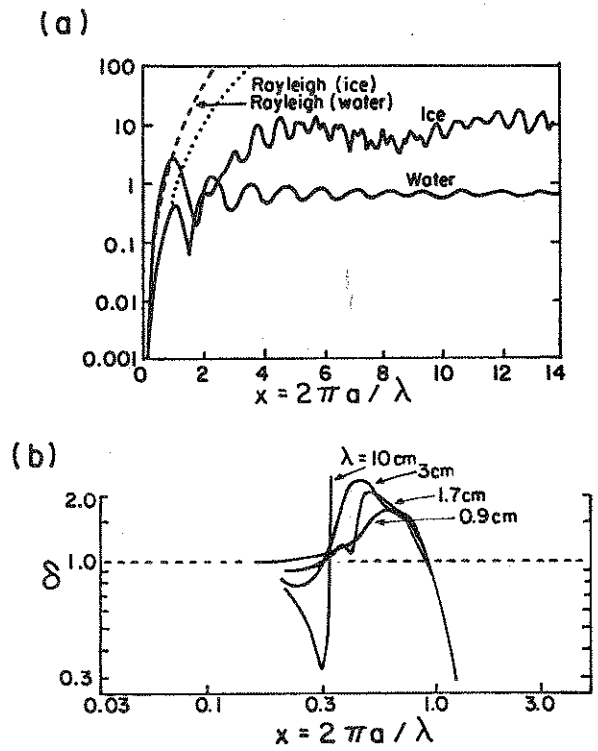


**Figure 5.29** (a) Backscattering efficiency for ice and water at $0^oC$ as a function of size parameter. The Rayleigh approximation is indicated for both phases. (b) Ratio of the Lorenz–Mie backscattering to Rayleigh backscattering for water spheres as a function of $x$ (adapted from Gunn and East, 1954).

the polarizer is $I_r$. The ratio of these measured intensities, namely

$$\delta = \frac{I_r}{I_\ell}$$

is the depolarization ratio. The physical interpretation of $\delta$ is clear when we consider the properties of $I_r$ and $I_\ell$ in more detail. To do so, consider a linearly polarized transmitted pulse which we represent by the Stokes vector

$$\mathbf{I}_o = \begin{pmatrix} 1 \\ 1 \\ 0 \\ 0 \end{pmatrix} \tag{5.66}$$



Suppose this pulse, backscattered by particles with properties that enable us to use (5.41), is passed through an ideal polarizing filter placed in front of the detector. In matrix form, the detected Stokes vector is

$$\mathbf{I} = \mathbf{M}_{\ell,r}\mathbf{P}\mathbf{I}_o \tag{5.67}$$

where $\mathbf{M}_{\ell,r}$ are the Mueller matrices as discussed in Section 2.3 relevant to the parallel [equation (2.40)] and perpendicular orientation of the polarizer, $\mathbf{P}$ is given by (5.41) and $\mathbf{I}_o$ by (5.66). With simple matrix algebra, it can be shown that

$$\delta = \frac{S_{11} - S_{22}}{S_{11} + S_{22}} \tag{5.68}$$

for the depolarization ratio. Since $S_{11} = S_{22}$ for spherical particles, $\delta = 0$. Thus $\delta$ may be thought of as a measure of the departure of the scatterer from sphericity.

A number of studies attempt to quantity relationships between $\delta$ and the size and shape of ice crystals, and the ratio of water mass to ice mass. An example of the use of $\delta$ in the study of cirrus clouds is provided in Fig. 5.30. This diagram is taken from the work of Sassen et al. (1985). It is a height–time display of $\delta$ derived from a vertically pointing lidar. The near–zero values of $\delta$ at the bottom of the cirrostratus cloud is indicative of supercooled liquid water spheres, and the presence of these droplets was confirmed by in situ measurements.

### *$Z_{DR}$ Ratios*

The backscattering ratio $Z_{DR}$ is used in the analyses of radar reflectivities to study the microphysics of precipitating clouds. Examples of these applications are presented in more detail in Chapter 8. Here we will try to show how $Z_{DR}$ is related to the phase matrix. In the operation of a dual polarization radar, as opposed to lidar, two linearly polarized pulses are transmitted with the directions of the polarization orthogonal to each other. One direction is referred to as the vertical although this is not necessarily the local vertical[8]. The

[8] Using the nomenclature adopted for our lidar example, both $I_{VV}$ and $I_{HH}$ are equivalent to the parallel component $I_\ell$ as the polarization of the detected signal is parallel to the polarization of the transmitted signal in both cases. For radar, the scattering plane is taken to be the vertical plane and the direction parallel to this plane is referred to as the vertical component (see footnote, p 192).

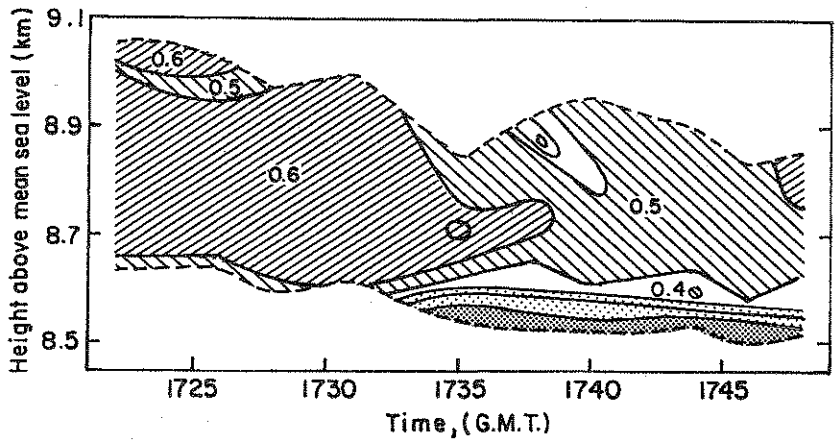


**Figure 5.30** Height versus time display of the depolarization ratio from vertically pointing lidar measurements. A gradual water–to–ice cloud transformation is shown by the decreasing stippling (increasing values of $\delta$) above cloud base. The cloud boundaries (dashed lines) derived from the $\delta$ analysis often do not correspond to the actual cloud boundaries (from Sassen et al., 1985).

second direction is referred to as the horizontal polarization. We use $I_{VV}$ for vertically polarized transmitted and received intensities and $I_{HH}$ for horizontally polarized intensities that are also transmitted and received. Using arguments similar to those presented earlier,

$$\mathbf{I}_{VV,HH} = \mathbf{M}_{V,H}\mathbf{P}\mathbf{I}_{o,V,H} \tag{5.69}$$

where $V$ is synonymous with $\ell$ and $H$ with $r$. The Stokes vectors of the transmitted pulses are

$$\mathbf{I}_{o,V} = \begin{pmatrix} 1 \\ 1 \\ 0 \\ 0 \end{pmatrix}, \quad \text{and} \quad \mathbf{I}_{o,H} = \begin{pmatrix} 1 \\ -1 \\ 0 \\ 0 \end{pmatrix} \tag{5.70}$$

Defining

$$Z_{DR} = 10\log\frac{I_{HH}}{I_{VV}} \tag{5.71}$$



and using (5.41), the Mueller matrices specified by (2.40) and the matrix expression immediately above (2.40) with $\psi = \pi/2$, then

$$Z_{DR} = 10\log[\frac{S_{11} - 2S_{12} + S_{22}}{S_{11} + 2S_{12} + S_{22}}] \tag{5.72}$$

which is expressed in units of $dB$. For spherical particles, or for randomly oriented nonspherical particles (tumbling hail for example), $I_{HH} \approx I_{VV}$ and $Z_{DR} = 0$. In precipitating regions of clouds, elongated raindrops tend to be preferentially orientated. We have tacitly assumed that dipoles are spherical in shape. Raindrops illuminated by centimeter wavelength microwave radiation may be thought of as nonspherical dipoles with a larger dipole moment parallel to the long axis of the drop (and aligned horizontally) than parallel to the short axis of the drop (and aligned vertically). This results in larger amounts of backscattering for horizontally polarized radiation than for vertically polarized radiation so that $I_{HH} > I_{VV}$. Thus $Z_{DR} > 0$ for rain drops. The larger the drop impling heavier rainfall, the more asymmetric it becomes. The more asymmetric the geometry of the drop, the larger is the value of $Z_{DR}$ (Fig. 5.31).

### *Circular Depolarization Ratios*

Another example of how we may use the polarization properties of particle backscatter applies to radars that transmit circularly polarized pulses. Suppose that the radar transmits a left–circularly polarized pulse. Backscattering by spheres returns a right circularly polarized pulse. Since any given polarization (including linear polarization, see Section 2.4) can be thought of as a mixture of left– and right–hand circular polarization, the scattering by irregular particles produces a component that has some degree of left–hand polarization as well as right–hand polarization. We can conveniently represent this mixture in terms of the circular depolarization ratio (CDR, again in units of dB)

$$CDR = 10\log(\frac{I_{LH}}{I_{RH}})$$

where $I_{LH}$ and $I_{RH}$ are the detected return powers for left–hand (LH) and right–hand (RH) circular polarization assuming the transmitted pulse is left–circularly polarized. For water droplet clouds, $I_{LH}$ is several orders of magnitude less than $I_{RH}$ yielding corresponding values of CDR that are less than about –25 dB. Ice clouds

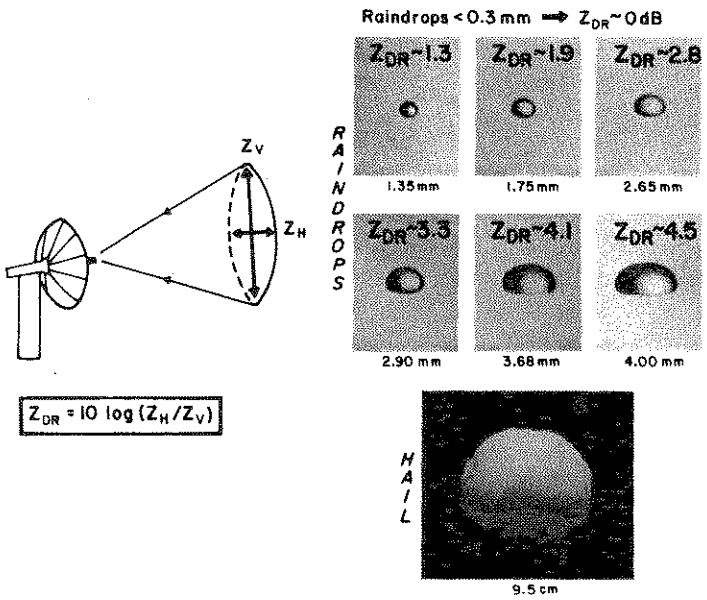


**Figure 5.31** Summary of typical $Z_{DR}$ values for raindrops of various sizes and hail. The black arrows on the hail represent its tumbling motions as it falls. Sizes are the median volume diameter (from Wakimoto and Bringi, 1988).

and clouds composed of larger, more oblate droplets are characterized by CDR values in the range between −15 to −25 dB whereas melting aggregate particles have values of CDR around −10 to −5 dB. Rarely does CDR exceed about −5 dB for naturally occurring scatterers at radar wavelengths. By contrast, the backscattering of circularly polarized radiation from an axial particle, like a piece of chaff, becomes linearly polarized along the direction of the long axis of the chaff. A linearly polarized beam can be decomposed into RH and LH circularly polarized components of equal amplitude in which case the value of CDR is 0 dB. CDR for chaff, therefore, differs significantly from the CDRs associated with scattering by cloud particles. Because of this difference, the chaff backscattering signal can be readily distinguished from the cloud particle scattering. This property provides a way of using chaff as a tracer of air motions inside clouds and thus offers potential for studying venting processes of boundary–layer pollutants by clouds or for studying the entrainment of surrounding air into clouds. Figure 5.32 is a visualization of the three–dimensional distribution of cloud volumes characterized



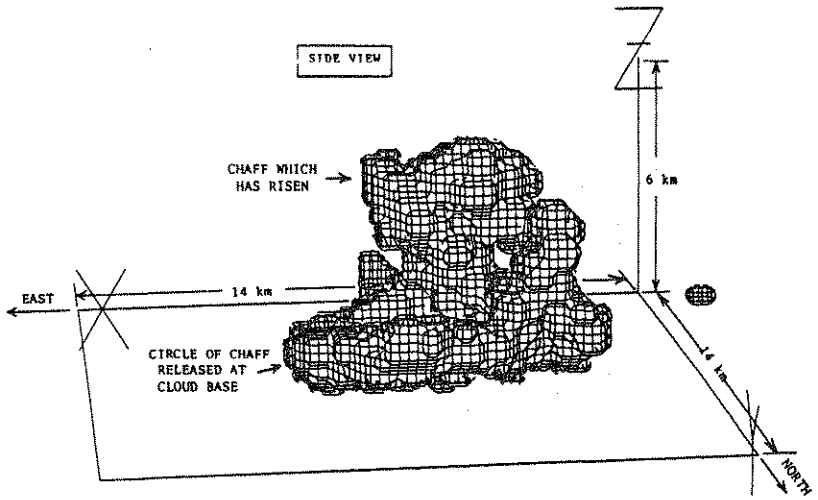


**Figure 5.32** A vertical cross–section of the distribution of chaff in a convective cloud. The chaff was released at cloud base in a circle and rose into the cloud by convection (Martner 1990, private communication).

by values of $CDR > -5$dB after chaff was released from an aircraft at the base of a convective cloud. This diagram shows the surface of chaff in the cloud and indicates how it rose in towers primarily on the southwest side of the cloud in strong and persistent updrafts.

## 5.8 Notes and Comments

5.1. A discussion of polarized light in the atmosphere, and in a Rayleigh atmosphere specifically, is given in Coulson (1988).

An account of Haidinger's Brush, and an experiment to observe it, is contained in the book of Minneart (1954) as well as in Kliger et al. (1990).

5.2. The discussion of scattering by a two dipole particle follows Bohren (1987).

The discrete dipole approximation (DDA) as a method for calculating the scattering by nonspherical particles was first proposed by Purcell and Pennypacker (1973). A number of studies since then have appeared in the literature, including the work of Singham and

Bohren (1988), Draine (1988), Flatau et al. (1990), and Goedecke and O'Brien (1988), among others. Tests of the method against analytical solutions have also been reported (e.g., Goodman et al., 1991; Evans and Vivekanandrum, 1990). Computational constraints have limited its application to particles characterized by small size parameters ($x \approx 5$, say). Thus the approach is well suited to study particle scattering for microwave radiation. The studies of Evans and Vivekanandan (1990) and Dungey and Bohren (1992) use DDA to examine the backscattering properties of nonspherical particles illuminated by microwave radiation. Goedke and O'Brien (1988) also use the method to model the scattering by irregular ice particles at microwave radiation. Evans and Stephens (1992) apply the DDA to examine the feasibility of using microwave scattering for remotely sensing ice clouds.

An important extension to the method is provided in the work of Goodman et al. (1991) who employ fast Fourier transform procedures to extend the applicability of the DDA out to size parameters of about 15.

A somewhat related, but nonetheless different, method of calculating scattering by particles of complex geometry is that of Fuller and Kattawar (1987) who developed a solution for light scattering by clusters of spheres.

5.3. An interesting piece of history is associated with the Poisson spot. In 1818, when Augustin Fresnel submitted his wave theory of diffraction, Simeon Poisson attempted to contradict Fresnel's explanation. Poisson deduced from the wave theory that a maximum should be observed on the axis directly behind a circular stop. He believed that his deduction would disprove the wave theory. At a later time Arago performed an experiment and found the spot; instead of dismissing a theory for diffraction, therefore, Poisson's calculations ironically reinforced it.

5.4. The method of ray tracing provides a way of calculating the scattering properties of irregular particles that are much larger in size than the wavelength of illumination. This method is not described in this book and the interested reader is referred to the work of Takano and Liou (1989) for examples of the application of this approach to the scattering by hexagonal ice crystals.

5.5. The ADT formulas (5.55) and (5.58) are indeed most convenient. van de Hulst (1957) qualifies his ADT results as "..one of the most useful formulae in the whole domain of Mie theory, because it



describes the salient features of the extinction curve, not only for m close to 1 but even for m values as large as 2."

5.6. The historical perspective of the solution to scattering by spheres has recently been revisited by Logan (1990). Other historical perspectives and anecdotes are contained in selected articles in a special issue of Applied Optics (November 20, 1991). Logan recalls the significant contributions to this problem by Clebsch in a remarkable paper published in 1863 and the solution of Lorenz reported in 1890 which is identical to that presented nearly 20 years later by Mie and Debye after Mie.

Clebsch sought to derive the response of a vector wave at the surface of a curved reflector. Maxwell's famous papers in 1864 and 1873 and Hertz's vindication of Maxwell's theory were still in the future when Clebsch began his study. Clebsch constructed the solutions of the scalar wave equation as an infinite series of terms involving spherical Bessel functions which he had invented for this purpose before Bessel. The solution to the vector wave equation was also developed. It was his wish that his analysis would enable him to deduce the laws of reflection from a spherical mirror by both longitudinal and transverse elastic waves from the solution of the boundary–value problem for elastic waves. The series were so complex that he was unable to derive any information from them except in the case of a sphere that was small compared to the wavelength. We now call this Rayleigh scattering.

It is noteworthy that the influence of Clebsch's 1863 paper is found in the 1890 work of Lorenz. In contrast to Clebsch, Lorenz noted that longitudinal waves should be excluded in studies of the propagation of light. The theory of light employed by Lorenz turns out to be mathematically identical to the Maxwell equations and he arrived at the identical solution to that presented by Mie. Within this historical perspective, Kragh (1991) suggests that the basic theory of plane wave scattering by spheres be called "Lorenz–Mie" theory and this is the terminology adopted in this book.

The numerical features of the Lorenz–Mie solutions are well described by Dave (1968) and Wiscombe (1980), and useful references are cited therein.

5.7. A review of particle backscattering, with an emphasis on the calculation of this backscatter, is provided by Bohren (1991). The method of DDA is mentioned in that paper and studies that employ this method to study backscatter were mentioned under 5.3.

The recent theoretical developments of Fuller and Kattawar (1987) for clusters of spheres were used by Muinonen and Lumme (1991) in which they propose a mechanism associated with coherent scattering between the spheres of the cluster to explain the observed polarization signatures of scattered starlight.

## 5.9 Problems

5.1. Explain or interpret the following:

a. Unpolarized radiation scattered by spherical particles much smaller than the wavelength of incident radiation becomes polarized.

b. A wind profiler antenna of 135 elements is capable of measuring wind to a greater range than an antenna of 35 elements.

c. On rare occasions the moon appears blue. Assuming that this is due to selective scattering by spheres of index of refraction 1.33, define an upper limit to the radius of the sphere? (You may use Fig. 5.16 to answer this question).

d. Under steady haze conditions, mountains viewed to the west during the morning hours appear clearer than the same mountains viewed in the afternoon.

e. Smoke from an automobile appears blue against a dark background but yellow against bright objects.

f. Why is sunlight observed at 90 degrees to the direction of the sun highly polarized? Why is the amount of polarization not 100%?

g. Under most circumstances, the single scatter albedo (the ratio $Q_{sca}/Q_{ext}$) for large particles approaches 0.5. Under which circumstances do you think this albedo is smaller than 0.5 for large particles?

5.2. Rayleigh scattering problem:

a. From (5.33) and (5.39), show that the scattered intensity at angle $\Theta$ is

$$I(\Theta) = I_o \frac{C_{sca}}{R^2} \frac{P(\Theta)}{4\pi}$$

and that the cross-sectional area per molecule is

$$C_{sca} = \frac{|\alpha|^2 128\pi^5}{3\lambda^4}$$

for Rayleigh scattering (note $\epsilon_o$ is replaced by the factor $1/4\pi$).



b. Using the Clausius–Mosotti relationship, calculate the scattering cross-section of molecules at 0.3, 0.5 and 0.7 $\mu$m assuming $N = 2.55 \times 10^{19}$ molecules per cubic centimeter, which is a typical value at sea level and

$$(m-1)\times 10^8 = 6.4326\times 10^3 + \frac{2.94981\times 10^6}{146-\lambda^{-2}} + \frac{2.554\times 10^4}{41-\lambda^{-2}}$$

for air where $\lambda$ is in $\mu$m.

c. If you assume that the variation of the density of air with altitude follows the variation of pressure with altitude $p = p_o \exp(-z/H)$, show that the Rayleigh optical depth, measured from the top of the atmosphere to level $z$ is directly proportional to the pressure at $z$. [*For later problems and for purposes of comparison, a parameterization of the Rayleigh optical depth as a function of wavelength (in microns) and altitude z (in kilometers) is*

$$\tau_{Ray}(\lambda, z) = 0.0088\lambda^{(-4.15+0.2\lambda)}[e^{-0.1188z-0.00116z^2}]$$

*(after Maggraf and Griggs (1969).]*

5.3. A plane wave electric field may be expressed as

$$\mathcal{E} = \mathcal{E}_o \exp\{-i(kr - \omega t)\}.$$

a. In the following diagram, the surface of constant phase emerging from two dipoles arrives at location 1 at a different time than at location 2. Convert this time difference into a phase difference. Express your answer in terms of the separation of the dipoles $d$ and angle of incidence $\gamma$.

b. Combine the proceeding answer with a similar expression for the difference in the phase between waves scattered from 1 and 2 arriving a distant detector at an angle $\Theta$ to the incoming plane wave. Show that the wave fronts are in phase whenever $\Theta = 0°$ (i.e., for the geometry of forward scattering).

5.4. Assume that a particle of diameter $d$ is approximated in a simple way as for Problem 5.3 and that dipoles are non-interacting. For a wave incident on this particle along a direction normal to a line that separates these dipoles (i.e., for $\gamma = 0$), derive an